Appendices

Appendix I

```
for k=1:27
   filename=sprintf('F:/experiments/stretching skin and mouse grafted skin/normal skin 1608 to 1708/in vivo stretching and flexing skin/flexing in vivo/in vivo skin inside bp380surface0um.tif',k);
   M=double(imread(filename));
   bp380=M;
   filename=sprintf('F:/experiments/stretching skin and mouse grafted skin/normal skin 1608 to 1708/in vivo stretching and flexing skin/flexing in vivo/in vivo skin inside bg39 surface0um.tif',k);
   M=double(imread(filename));
   bg39=M;
   bp380threshold=zeros(512);
   for i=1:512
      for j=1:512
         if bp380(i,j) > 70
            bp380threshold(i,j)=bp380(i,j);
         end
      end
   end
   Im(1:512,1:512,1)=bp380threshold;
   Im(1:512,1:512,2)=bg39-bp380;
   Im(1:512,1:512,3)=zeros(1:512,1:512);
   %Fig(k);
   %image(uint8(Im));
   filename=sprintf('F:/experiments/stretching skin and mouse grafted skin/normal skin 1608 to 1708/in vivo stretching and flexing skin/flexing in vivo/in vivo skin inside bp380surface0umoverlap.tif',k);
   imwrite(uint8(Im),filename,'tif');
end
```

Appendix II

```
clc
clear
% Intensity summary
for i=1:9
   filename=sprintf('D:/FRAP/frap and aspf 04042007/aspf site1.mdb/aspf site1%01d.tif',i);
   M=imread(filename);
   Im1(i,:,:)=M;
   s1(i)=sum(sum(Im1(i,:,:)));
end
% Normalisation
sminimum1=min(s1);
for i=1:9
   ss1(i)=s1(i)-sminimum1;
end
smaximum1=max(ss1);
for i=1:9
   sss1(i)=ss1(i)/smaximum1;
end
Fig(1);
x1=0:2:16;
plot(x1,sss1,'b');hold on;
%Derivision
for i=2:8
   derivesss1=(sss1(i+1)-sss1(i-1))/2;
end
%Plot
xderive=1:7;
plot(xderive,derivesss1);hold off;

for i=1:9
   filename=sprintf('D:/FRAP/frap and aspf 04042007/aspf site2.mdb/aspf site2%01d.tif',i);
   M=imread(filename);
   Im2(i,:,:)=M;
   s2(i)=sum(sum(Im2(i,:,:)));
```

```
end
sminimum2=min(s2);
for i=1:9
   ss2(i)=s2(i)-sminimum2;
end
smaximum2=max(ss2);
for i=1:9
   sss2(i)=ss2(i)/smaximum2;
end
x2=0:2:16;
plot(x2,sss2,'r');hold on;

for i=1:9
   filename=sprintf('D:/FRAP/frap and aspf 04042007/aspf site3.mdb/aspf site3%01d.tif',i);
   M=imread(filename);
   Im3(i,:,:)=M;
   s3(i)=sum(sum(Im3(i,:,:)));
end
sminimum3=min(s3);
for i=1:9
   ss3(i)=s3(i)-sminimum3;
end
smaximum3=max(ss3);
for i=1:9
  sss3(i)=ss3(i)/smaximum3;
end
Fig(2);
x3=0:2:16;
plot(x3,sss3,'g');hold on;
for i=1:9
   filename=sprintf('D:/FRAP/frap and aspf 04042007/aspf site4.mdb/aspf site4%01d.tif',i);
   M=imread(filename);
   Im4(i,:,:)=M;
   s4(i)=sum(sum(Im4(i,:,:)));
end
```

```
sminimum4=min(s4);
for i=1:9
   ss4(i)=s4(i)-sminimum4;
end
smaximum4=max(ss4);
for i=1:9
   sss4(i)=ss4(i)/smaximum4;
end
x4=0:2:16;
plot(x4,sss4,'k');hold on;

for i=1:9
   filename=sprintf('D:/FRAP/frap and aspf 04042007/aspf site5.mdb/aspf site5%01d.tif',i);
   M=imread(filename);
   Im5(i,:,:)=M;
   s5(i)=sum(sum(Im5(i,:,:)));
end
sminimum5=min(s5);
for i=1:9
   ss5(i)=s5(i)-sminimum5;
end
smaximum5=max(ss5);
for i=1:9
   sss5(i)=ss5(i)/smaximum5;
end
x5=0:2:16;
plot(x5,sss5,'m');hold on;
for i=1:9
   filename=sprintf('D:/FRAP/frap and aspf 04042007/aspf site6.mdb/aspf site6%01d.tif',i);
   M=imread(filename);
   Im6(i,:,:)=M;
   s6(i)=sum(sum(Im6(i,:,:)));
end
sminimum6=min(s6);
for i=1:9
```

```
    ss6(i)=s6(i)-sminimum6;
end
smaximum6=max(ss6);
for i=1:9
    sss6(i)=ss6(i)/smaximum6;
end
x6=0:2:16;
plot(x6,sss6,'y');hold off;
axis([-4 20 0 1])
xlabel('Depth');
ylabel('Intensity');
title('ASPF of 40X oil immersion objective lens');
legend('site1','site2','site3','site4','site5','site6');
```

Appendix III

Prolate spheroid formula and data fittin formula in Prism4

a is the radius of the circle and h is the height of the prolate spheroid

1. for a equals to h/2

$$fl\_cyl = 1 - f_{b0} \cdot \left(\sqrt{\frac{\tau_2}{\pi}} \cdot e^{\left(-\frac{1}{\tau_2}\right)} + erf\left(\frac{1}{\sqrt{\tau_2}}\right) - \sqrt{\frac{\tau_2}{\pi}} \right)^3 \qquad 1)$$

$$\tau_2 = \frac{D \cdot t}{r_0^2 \cdot \left(\frac{\pi}{4}\right)^{\frac{2}{3}}}$$

where , D is diffusion coefficient, t is time, r0 is the radius of the photo-bleached cylindrical volume (with height h equal to 2r0) and fb0 is the extent of photo-bleaching inside cube/prolate spheroid (fb0=1 for 100% photo-bleaching). D and fb0 are two fitting parameters.

In Prism4 fitting program

Y=(1-a*(sqrt(b*x1/(r0^2*0.7854^(2/3))/3.1416)*exp(-1/

(b*x1/(r0^2*0.7854^(2/3))))+erf(1/(sqrt(b*x1/(r0^2*0.7854^(2/3))))-

sqrt(b*x1/(r0^2*0.7854^(2/3)) /3.1416))^3)*c

a bleach percentage

b diffusion coefficient

c original intensity

x1= x-T0; T0=0.5101 (19pixels glycerol),T0=0.5294 (21pixels glycerol);T0=0.5583(24pixels glycerol)

T0=0.5005 (19pixels skin)

r0^2=1 μm^2 (19pixels glycerol and skin); 1.21(21pixels glycerol); 1.5876(24pixels glycerol)

Fitting length: number 13 to 262 data in excel data sheet for each bleached area (exclude the pro-bleach ten images' intensity and began from the third second sample time after bleaching)

2. for a not equals to h/2

$$fl\_cyl = 1 - f_{b0} \cdot \left(\sqrt{\frac{\tau_2}{\pi}} \cdot e^{\left(-\frac{1}{\tau_2}\right)} + erf\left(\frac{1}{\sqrt{\tau_2}}\right) - \frac{\tau_3}{\pi} \cdot \left(\sqrt{\frac{\tau_3}{\pi}} \cdot e^{\left(-\frac{1}{\tau_3}\right)} + erf\left(\frac{1}{\sqrt{\tau_3}}\right) - \sqrt{\frac{\tau_3}{\pi}} \right) \right) \qquad 2)$$

$$\tau_2 = \frac{D \cdot t}{r_0^2 \cdot \left(\frac{\pi}{4}\right)^{\frac{2}{3}}} \quad \tau_3 = \frac{D \cdot t}{\left(\frac{h}{2}\right)^2}$$

where , , h=3 μm, h/2=1.5 μm

In Prism4 fitting program

Y=(1-a*(sqrt(b*x1/(r0^2*0.7854^(2/3))/3.1416)*exp(-1/
(b*x1/(r0^2*0.7854^(2/3))))+erf(1/(sqrt(b*x1/(r0^2*0.7854^(2/3))))-
sqrt(b*x1/(r0^2*0.7854^(2/3))/3.1416))^2*(sqrt(b*x1/1.5^2)*exp(-
1/(b*x1/(1.5^2)))+erf(1/(sqrt(b*x1/(1.5^2))))-sqrt(b*x1/(1.5^2) /3.1416)))*c

a bleach percentage

b diffusion coefficient

c original intensity

x1= x-T0; T0=0.5101 (19pixels glycerol),T0=0.5294 (21pixels glycerol);T0=0.5583(24pixels glycerol)

T0=0.5005 (19pixels skin)

r0^2=1μm^2 (19pixels glycerol and skin); 1.21(21pixels glycerol); 1.5876(24pixels glycerol)

Fitting length: number 13 to 262 data in excel data sheet for each bleached area

Cubic formula and data fitting formula in Prism4

a is the side of the cube and h is the height of the square

1. a equals to h/2

$$fl\_cube = 1 - f_{b0} \cdot \left(\sqrt{\frac{\tau_1}{\pi}} \cdot e^{\left(-\frac{1}{\tau_1}\right)} + erf\left(\frac{1}{\sqrt{\tau_1}}\right) - \sqrt{\frac{\tau_1}{\pi}} \right)^3 \qquad 3)$$

where $\tau_1 = \frac{D \cdot t}{a^2}$

In Prism4 fitting program

Y=(1-a*(sqrt(b*x1/(r0^2*3.14))*exp(-1/(b*x1/r0^2))+erf(1/(sqrt(b*x1/ro^2)))-
sqrt(b*x1/(r0^2*3.14)))^3)*c

a bleach percentage

b diffusion coefficient

c original intensity

x1=x-0.9444

r0^2=1μm^2 (19pixels skin)

2. a not equal to h/2

$$fl\_cube = 1 - f_{b0} \cdot \left(\sqrt{\frac{\tau_1}{\pi}} \cdot e^{\left(-\frac{1}{\tau_1}\right)} + erf\left(\frac{1}{\sqrt{\tau_1}}\right) - \frac{\tau_1}{\pi} \cdot \left(\sqrt{\frac{\tau_3}{\pi}} \cdot e^{\left(-\frac{1}{\tau_3}\right)} + erf\left(\frac{1}{\sqrt{\tau_3}}\right) - \sqrt{\frac{\tau_3}{\pi}} \right) \right) \quad 4)$$

where $\tau_1 = \frac{D \cdot t}{a^2}$, $\tau_3 = \frac{D \cdot t}{\left(\frac{h}{2}\right)^2}$, h=3 μm, h/2=1.5 μm

In Prism4 fitting program

Y=(1-a*(sqrt(b*x1/r0^2*3.14)*exp(-1/(b*x1/r0^2))+erf(1/(sqrt(b*x1/r0^2)))-sqrt(b*x1/r0^2*3.14))^2*(sqrt(b*x1/(1.5^2*3.14))*exp(-1/((b*x1/1.5^2)))+erf(1/(sqrt(b*x1/1.5^2)))-sqrt(b*x1/(1.5^2*3.14))))*c

a bleach percentage

b diffusion coefficient

c original intensity

x1=x-0.9444

r0^2=1μm^2 (19pixels skin)

Imaging of zinc oxide nanoparticle penetration in human skin *in vitro* and *in vivo*

Andrei V. Zvyagin
Xin Zhao
Macquarie University
Department of Physics
Centre of MQ Photonics
Sydney, NSW 2109, Australia

Audrey Gierden
Université Claude Bernard Lyon
Institut des Sciences Pharmaceutiques et Biologiques
Lyon, France

Washington Sanchez
Justin A. Ross
Michael S. Roberts
The University of Queensland
School of Medicine
Therapeutics Research Unit
Princess Alexandra Hospital
Australia

Abstract. Zinc oxide (ZnO-nano) and titanium dioxide nanoparticles (20 to 30 nm) are widely used in several topical skin care products, such as sunscreens. However, relatively few studies have addressed the subdermal absorption of these nanoparticles *in vivo*. We report on investigation of the distribution of topically applied ZnO in excised and *in vivo* human skin, using multiphoton microscopy (MPM) imaging with a combination of scanning electron microscopy (SEM) and an energy-dispersive x-ray (EDX) technique to determine the level of penetration of nanoparticles into the sub-dermal layers of the skin. The good visualization of ZnO in skin achieved appeared to result from two factors. First, the ZnO principal photoluminescence at 385 nm is in the "quiet" spectral band of skin autofluorescence dominated by the endogenous skin fluorophores, i.e., NAD[P]H and FAD. Second, the two-photon action cross section of ZnO-nano [$\sigma_{ZnO}^{(TPEF)} \sim 0.26$ GM; diameter, 18 nm] is high: ~500-fold of that inferred from its bulk third-order nonlinear susceptibility [$\mathrm{Im}\,\chi_{ZnO}^{(3)}$], and is favorably compared to that of NAD[P]H and FAD. The overall outcome from MPM, SEM, and EDX studies was that, in humans *in vivo*, ZnO nanoparticles stayed in the stratum corneum (SC) and accumulated into skin folds and/or hair follicle roots of human skin. Given the lack of penetration of these nanoparticles past the SC and that the outermost layers of SC have a good turnover rate, these data suggest that the form of ZnO-nano studied here is unlikely to result in safety concerns. [DOI: 10.1117/1.3041492]

Keywords: nonlinear optical microscopy; nanoparticle toxicity; zinc oxide; transdermal permeability; multiphoton microscopy.

Paper 08185R received Jun. 13, 2008; revised manuscript received Sep. 5, 2008; accepted for publication Oct. 20, 2008; published online Dec. 23, 2008.

1 Introduction

Nanomaterials including nanoemulsions, nanosomes, and nanoparticles are employed as active components[1,2] and delivery vehicles[3,4] in cosmetics and medicine. One example of a nanotechnology application is the widespread use of zinc oxide (ZnO-nano) and titanium dioxide (TiO_2) nanoparticles as ingredients in cosmetic and sun-blocking creams. These nanomaterials are efficient absorbers of the ultraviolet (UV) radiation: ZnO absorbs both UVA (400 to 320 nm) and UVB (320 to 290 nm) radiation and reemits them as less damaging UVA or as visible fluorescence (and is dictated by the need to minimize skin damage due to UV light and potential consequences such as skin cancer). The use of these sun-blocking creams is widespread in Australia, where over 250,000 people are diagnosed with nonmelanoma skin cancer, and over 8000 with melanoma annually.[5]

The upper size limit for ZnO and TiO_2 nanoparticles is dictated by the aesthetic marketing value of transparent sun-blocking creams. Transparency is achieved by reducing scattering efficiency of ZnO particles, which are normally white and visible, by using a nanoparticle size of less than 30 nm, its transparency threshold.[6] An inevitable question then is whether there a potential toxicity of these nanoparticles whose size may be small enough to allow them to penetrate the skin. The extent of nanoparticles penetration through the topmost layer of the skin, stratum corneum (average thickness, less than 20 μm) into the viable epidermis, is hotly debated. As an illustration, the studies of Alvarez-Roman et al. shows no penetration through excised human skin.[6] In contrast, Ryman-Rasmussen[33] show extensive penetration of neutral, positively charged and negatively charged quantum dots through pig skin. *In vitro* cytotoxicity of ZnO-nano to epidermal (and, especially, epithelial) cells can occur and have been attributed to free radical generation (mainly via hydroxyl radicals formed through oxidation), causing adverse effects in isolated cell experiments.[8,9]

Conventional scanning electron microscopy (SEM), transmission electron microscopy and Franz cell penetration in-

Address all correspondence to: Andrei V. Zvyagin, Dept. of Physics, Centre of MQ Photonics, Macquarie Univ., Sydney, NSW 2109, Australia; Tel: +61 2 9850 7760; Fax: +61 2 9850 7760 8115; Email: azvyagin@ics.mq.edu.au

1083-3668/2008/13(6)/064031/9/$25.00 © 2008 SPIE

volve indirect or/and destructive sampling of skin that limits the experimental methods to *in vitro* observations. Optical microscopy of nanoparticle distribution in skin *in vivo* is precluded due to high scattering efficiency of the superficial layers of skin, especially human skin. Fluorescence confocal microscopy has enabled production of clear subsurface images of skin at depths down to ~100 μm at the micrometer resolution by way of "optical sectioning" thin layers of the specimen. The skin morphology contrast is derived from the skin autofluorescence, although often requires additional staining. The visibility of nanoparticles depends on their fluorescent properties, which limits the choice to the following materials: micro- and nanobeads impregnated with fluorescence dye molecules, photoluminescent nanomaterials, quantum dot (Qdot) structures,[10] and emerging nanocrystals with color centers.[11] Fabrication of nanobeads impregnated with fluorescent dye is difficult and they are prone to photobleaching. Qdots are cytotoxic, thus, posing hazard for *in vivo* applications on humans. Although silica Qdots are less cytotoxic, their photoluminescence (PL) degradation and complex passivation chemistry makes their application cumbersome and expensive.[12] PL materials, such as semiconductor metal oxides, are either toxic, radiation-inefficient (due to the indirect band gap structure), or rare. In contrast, ZnO-nano represents a promising nanomaterial that is widespread, inexpensive, and has proven to be suitable for cosmetic care and pharmacy. Its production is straightforward, yielding nanoparticle of various sizes and shapes, starting from 3 nm and larger.[7,13] ZnO material properties, including a direct wide bandgap (3.4 eV) electronic structure, and high exciton energy of 60 meV (compare to that of 25 meV of cadmium selenide), are very attractive for a new generation of electro-optic devices, e.g., light-emitting diodes and lasers in the UV spectral range. The wide bandgap of ZnO requires excitation at a wavelength of 320 nm in the UV spectral range, with principle emission at 385 nm, as shown in Fig. 1 (scattered squares graph). This excitation requirement is problematic for application of ZnO-nano in optical biomedical imaging. First, UV photons efficiently excite a number of intrinsic (endogenous) fluorophores in skin that produce a broadband autofluorescence background. Among these, nicotinamide adenine dinucleotide/nicotinamide adenine dinucleotide phosphate (NAD[P]H), flavin adenine dinucleotide (FAD), and porphyrins contribute 75, 25, and 2% to the skin autofluorescence, with their respective fluorescence bands centered at 425, 520, and 625 nm (Ref. 15) [also see Fig. 1(a)]. Second, UV radiation is heavily absorbed and scattered by the skin tissue, severely limiting imaging penetration depth. Hence, optical imaging of thick skin tissue using UV light is not practical.

It has been recently found that the zinc oxide structure is efficiently excited via a nonlinear optical process of simultaneous absorption of two or three photons under illumination by an ultrashort-pulse laser.[16] This shifts the ZnO excitation band to the infrared (IR) range, where the ultrashort-pulse laser sources predominantly operate, falling into the so-called therapeutic window, 600 to 1400 nm, wherein the maximum imaging penetration depth in tissue of ~200 μm is attainable. The increased penetration depth is due, first, to the markedly reduced absorption of the major tissue constituents, including proteins, hemoglobin, and melanin in the UV/visible spectral range, and the water transparency window; and, second, to the reduced scattering efficiency of skin tissue at longer wavelengths.

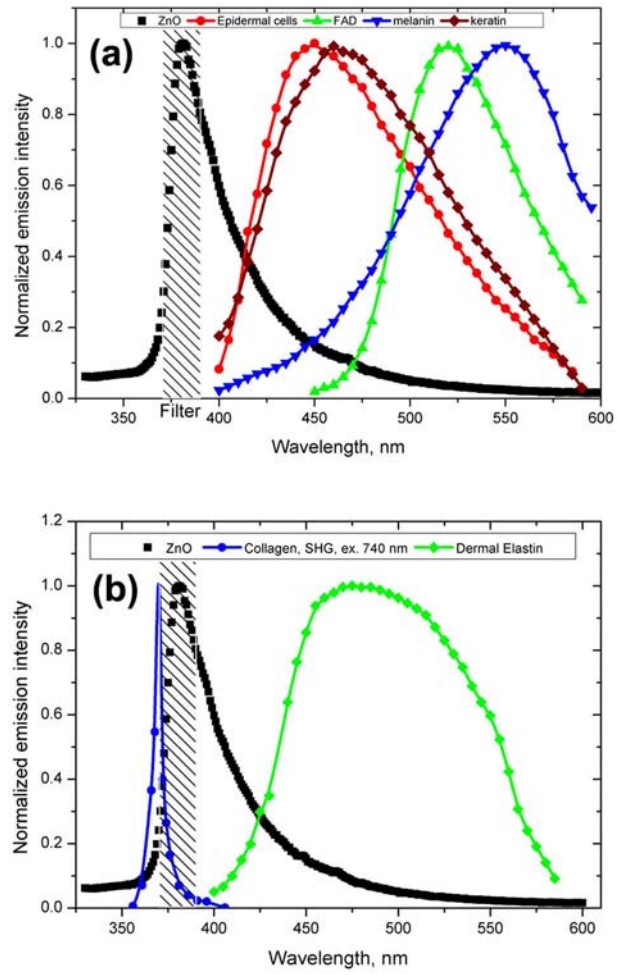

Fig. 1 Emission spectrum of ZnO-nano at an excitation wavelength of 320 nm (scatter plot, squares) superimposed on TPEF spectra of (a) epidermal cells (circles), similar to a spectrum of NAD[P]H; FAD (triangles); melanin (inverted triangles); keratin (diamonds), adapted from Ref. 14; and (b) elastin (diamonds), similar to collagen, adapted from Ref. 14; and the second-harmonic generation (SHG) spectrum of collagen calculated at a 740-nm fundamental wavelength. A dashed area designates FWHM of the bandpass filter BP380 used to discriminate ZnO PL signal against the skin autofluorescence.

In this paper, we communicate our results on application of multiphoton microscopy to study of ZnO nanoparticles penetration in human skin *in vitro* and *in vivo*. This is the first time, to the best of our knowledge, that the *in vivo* observation of inorganic PL nanoparticles in the morphology context of live cells and tissue has been reported. This will enable imaging of a new class of engineered nanostructures as applied to transdermal delivery and toxicology.

2 Materials and Methods

2.1 *Materials*

Dr. Lewinns' private formula (19% w/w) (Advanced Nanotechnology Ltd., WA, Australia) is comprised of 26 to 30-nm

mean size ZnO particles with preservatives of phenoxyethanol (0.3% w/w) and hydroxybenzoates (0.3% w/w) suspended in caprylic capric triglycerides.[17] These nanoparticles were fabricated by using the mechanochemical processing technology based on dry milling that induced chemical reactions through ball-powder collisions resulting in nanoparticle formation within a salt matrix. Particle size was determined by the chemistry of the reactant mixture, milling and heat treatment conditions.

For *in vivo* experiments, an area of 50 cm^2 of skin was selected on the forearm, cheek, shoulder, or feet of the subject and cleaned with ethanol. Four subjects of different ethnic background participated in this experiment: two Caucasian males, one Indian male, and a Chinese female aged 30 to 40, 40 to 50, and 25 to 30 yr, respectively.

For *in vitro* study, excised abdominal or breast human skin was obtained after plastic surgery.

2.2 *Sample Treatment*

Approximately 0.3 g of commercial Dr Lewinns' sun-blocking special formulation was applied evenly to the selected area of the human subjects and rubbed in for 5 min. The small amount was chosen arbitrarily to represent normal user application conditions. The area of application was small in comparison with the normal application of sunscreens for sun-blocking purposes. Subsequently, the treated area was noninvasively imaged using the multiphoton imaging system. A drop of water was applied to the region of skin being studied, followed by a 170-μm-thick microscope glass cover slip to ensure aberration-free imaging, and finally immersion oil between the coverslip and objective lens.

Images were acquired in three sessions: (1) immediately, (2) after 4 h, and (3) 24 h after the topical application, following washing. After session 1, the subject was allowed to move, as per usual daily routine. Session 3 was carried out following a shower at night, where the sun-blocking cream residue was washed away from the superficial layers of the skin. The rationale behind the times at which the images were carried out are as follows. Imaging immediately after application served as a control for time-lapse imaging. Imaging after 4 h was chosen as a representation of outdoors activities of the native population of southeast Queensland. The 24-h imaging was performed to verify whether prolonged exposure to sunscreens had any bearing on the ZnO penetration.

All experiments conducted on human subjects were done with approval of Princess Alexandra Hospital Research Committee (Approval No. 097/090, administrated by the University of Queensland Human Ethics Committee). Each subject gave written consent.

2.3 *Scanning Electron Microscope and Energy-Dispersive X-Ray Microanalysis*

We employed a Philips XL30 FEG scanning electron microscope (SEM), with a backscattered electron detector and an integrated energy-dispersive x-ray (EDX) microanalysis system. The following procedure was used for sample preparation for SEM/EDX imaging and microanalysis. The ZnO nanoparticle formulation was applied to the excised skin sample, and incubated for 2 to 24 h. Several skin patches were tape-stripped 10 to 20 times on the areas of interest, while the other patches remained untouched. These nanoparticle-treated skin samples were fixed in 2.5% glutaraldehyde solution, a requirement of the SEM facilities used and workplace health and safety protocols, prior to freeze drying. Before imaging, all the samples were vacuum-coated with a 20- to 50-nm carbon coating. Conductive paint was applied to the aluminium stub holder. The SEM was operated at a 15- to 20-kV acceleration voltage and high vacuum, demanding all organic tissue to be fixed and dried. Images were obtained at a 11.3-mm working distance (the distance between lens and the sample stage). The numerical aperture (NA) was 6, and coarse was 7 units in the standard microscope settings. Focus, brightness, and contrast were adjusted for each image.

The fixed skin was cut into small cubical shape blocks approximately 1 cm^3 and snap-frozen with a specially made copper press that had been dipped in liquid nitrogen for 5 min. The samples were further dipped while in the press in liquid nitrogen and then freeze-dried. The small freeze-dried skin samples were mounted on the SEM, and imaged immediately.

2.4 *Multiphoton Imaging*

In the multiphoton microscopy (MPM) imaging system (JenLab GmbH Schillerstraße 107745 Jena Germany), ultrashort-pulse excitation laser light was tightly focused onto a sample by using a high-NA oil-immersion microscope objective (40 $\times$, NA1.3). This resulted in an enormous instantaneous intensity in the femtoliter focal volume that elicited the material's nonlinear optical response. Two-photon excited fluorescence (TPEF) is one manifestation of this nonlinear process. The fluorescence emission is localized exclusively within the focal volume resulting in the inherent "optical sectioning" property of multiphoton microscopy.[18] The thickness of each optical section was determined by the axial transfer function of the optical multiphoton imaging system, which was measured to be 2 μm for our experimental configuration. The excitation light represented a pulsed femtosecond laser, which was a tunable, computer-controlled titanium-sapphire laser (MaiTai, Spectra Physics) whose wavelength was set to 740 nm. The laser pulsewidth and repetition rate was 85 fs and 80 MHz, respectively. The incident optical power was set to 20 and 30 mW in stratum corneum and epidermis, respectively. A focused laser spot was raster-scanned across the sample using two galvanometer mirrors. The excited fluorescence was collected by the same objective lens. A dichroic mirror transmitted fluorescence to the detection photomultiplier tube (PMT), while reflecting the IR laser excitation light. In the detection arm, the fluorescence was split between two channels terminated by two optical detectors (PMTs) following preselected spectral filters. A narrow-bandpass interference filter (BP380, Omega Optical) centered at 380 nm, with a FWHM of 20 nm, was inserted in channel 1 to selectively detect ZnO PL signal. In channel 2, a broad bandpass filter (BG39, Schott glass color filter) with a long-wavelength cutoff of 700 nm was employed to block the excitation laser light so that the skin autofluorescence emission was captured. An image was formed by recording detector signals versus the focal spot position in the sample. The two images from the two channels were overlaid at a postprocessing stage.

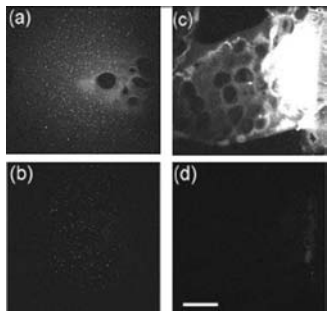

Fig. 2 MPM images: (a) and (b) ZnO-nano (scattered bright dots) the capric/caprilic oil film cast on a glass slide; (c) and (d) excised skin patch. Epidermal cellular architecture is clearly observable in (c). Images (a) and (c) and (b) and (d) are detected using the broadband (channel 1) and narrowband (channel 2) spectral filters, respectively. Scale bar 50 μm.

To optimize the spectral filter configuration in the detection arms, a preliminary imaging experiment using two samples was conducted. Sample 1 represented Dr Lewinns' cosmetic formulation diluted to a concentration of 0.005% and spin-coated on a glass slide to form nanoparticles and clusters. Sample 2 was a skin patch prepared, as already described in this section. The results of multiphoton imaging of these samples are presented in Fig. 2. Panels on the left- and right-hand-side columns show images of samples 1 and 2, respectively. The top and bottom images were obtained using the broadband (BG39) and UV narrowband (BP380) filters, respectively. Suppression of autofluorescence from caprylic/capric triglycerides solvent, visible as structured layout [Fig. 2(a)], is evident by comparing panels in Figs. 2(a) and 2(b). Likewise, the strong skin autofluorescence [Fig. 2(c)] is efficiently filtered by the UV narrowband filter [Fig. 2(d)]. The excised skin sample was deprived of NAD[P]H resulting in reduced autofluorescence intensity, probably dominated by FAD fluorescence.[14] Note that although the broadband emission in the visible spectrum of ZnO and ZnO-nano has been reported previously,[19] it was not observed in this study, probably owing to the high crystal quality of our ZnO-nano sample.

3 Results

Figure 3 shows our first *in vivo* images of human skin treated with the zinc oxide commercial formulation. Overlaid multiphoton images of human skin *in vivo* and ZnO-nano distribution, 4 hours after its topical application, are colorcoded green and red, respectively. *En face* optical sections of the skin are displayed from top left to bottom right at depths 0, 3, 14, 22, 30, and 48 μm from the skin surface designated S. The depth readout was corrected for the confocal parameter, calculated as $d_z=(z-z_0)n$, where $(z-z_0)$ denotes a difference between the axial position readout at a depth and top surface settings, and n denotes the mean refractive index of tissue, which was set to a mean value of 1.4 (Ref. 20). ZnO-nano patterns are clearly observable on the skin autofluorescence background, and especially pronounced on the topmost layers of the skin. Fine morphological details of unstained skin are clearly observable, e.g., cell structure in stratum granulosum (Fig. 3, bottom left panel), with dark nuclei and a granulated pattern in the cell cytoplasm, presumably, originated from NAD[P]H accumulated in mitochondria. As Fig. 3 shows, ZnO-nano predominantly remained on the topmost layer of SC within a several-micrometer layer (image panels S to 3 μm). The nanoparticle localization in the skin folds and dermatoglyph is clearly evident from Fig. 3 (14 μm to 30 μm). No penetration of ZnO-nano into the cells or extracellular space was observed.

Figure 4 shows images for the skin subdermal absorption of ZnO-nano after occupational exposure to the sunscreen formulation for various times. The skin of the three human subjects of different ethnical origins was imaged and analyzed using time-lapse *in vivo* MPM imaging of skin: shortly, 4 h

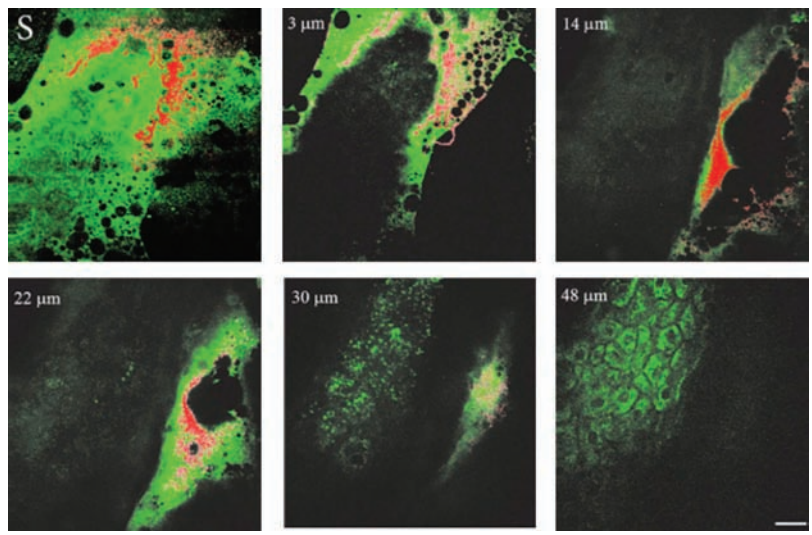

Fig. 3 Overlaid MPM images of human skin *in vivo* (color-coded green) and ZnO-nano distribution (color-coded red) 4 h after its topical application. *En face* optical sections of the skin are displayed from top left to bottom right at depths of 0, 3, 14, 22, 30, and 48 μm from the skin surface designed S and 3, 14, 22, 30, and 48 μm, respectively. Note ZnO localization in stratum corneum and in skin folds. No presence of nanoparticles in the stratum granulosum layer (ellipsoidal cells with dark nuclei) is observable. Scale bar 20 μm.

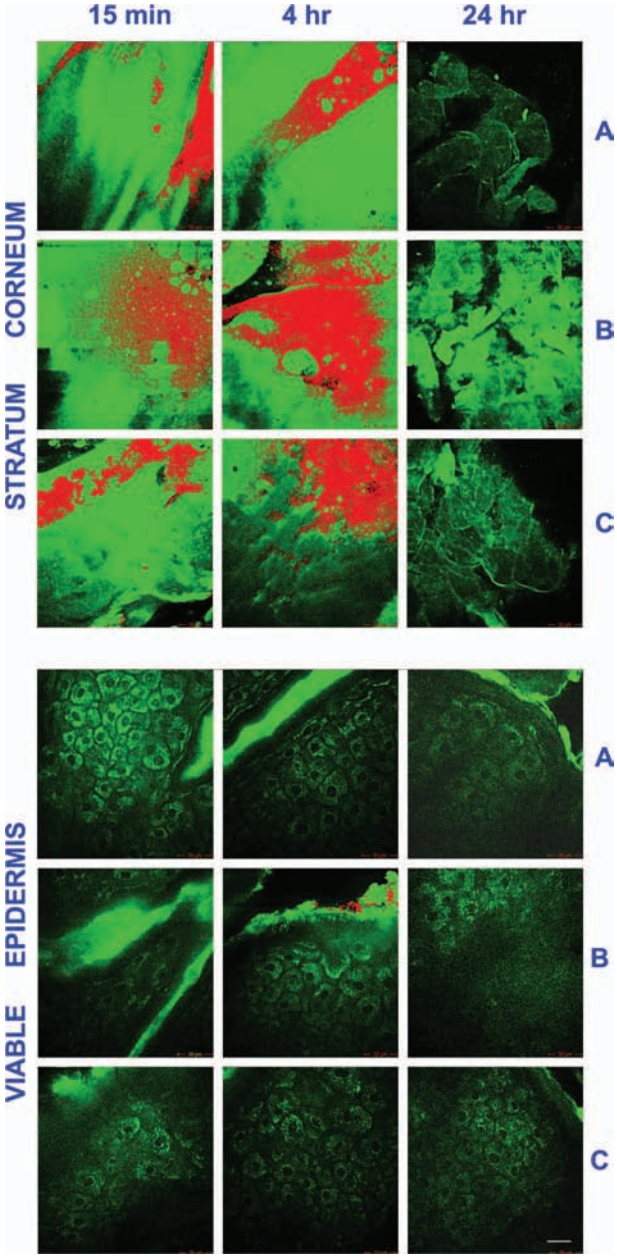

Fig. 4 Overlaid *in vivo* MPM images of ZnO-nano (color-coded red) distribution in human skin, forearm, dorsal side (color-coded green). Optical sections of stratum corneum and viable epidermis are grouped in two blocks. Each row displays images of three human subjects: Asian female, Chinese, aged below 30; Caucasian male, aged 30 to 40; and Indian male, aged 40 to 50, are designated by A, B, and C, respectively. Each column displays time-lapse image sequence acquired: 15 min, 4 h, 24 h, following the ZnO-formulation topical application. Scale bar 20 μm.

and 24 h after topical application of the formulation. No traces of ZnO were present in the viable epidermis (Viable Epidermis, Fig. 4), other than a well-confined island of ZnO in a skin fold (dark clearly outlined area) at 4 h after the sunscreen application in Caucasian skin, subject B. Images of SC acquired 24 h after sunscreen application show complete removal of sunscreen from skin, probably as a result of the daily shower routine exercised by each human subject in this

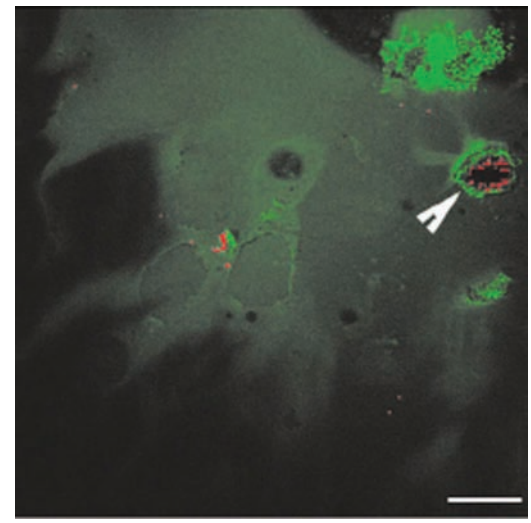

Fig. 5 Overlaid MPM images of the freshly (2 h) excised human skin (color-coded green) and ZnO-nano distribution (color-coded red) 4 hours after its topical application. An arrow points to the hair follicle canal, where a hair follicle shaft is not visible. ZnO formulation is localized around the hair follicle. Scale bar 20 μm.

experiment. In effect, this suggests ZnO-nano subdermal absorption after longer exposures is also unlikely.

MPM also enabled the investigation of alternative pathways of nanoparticle penetration, such as the appendages, as represented by the hair follicle canal. Since the hair follicle shaft can extend at a considerable depth in skin, 50 μm or greater, it can potentially represent an entry port of materials directly into the viable epidermis. Figure 5 shows an MPM cross-sectional image of the freshly (2 h) excised human skin topically treated with the sunscreen formulation. As described previously, no penetration of ZnO-nano is observable. At the same time, a prominent ZnO signal is noticeable at the perimeter of the hair follicle (white arrow). The hair shaft is not visible in the image. The sunscreen is localized in the hair follicle shaft without spreading to the neighboring cells and tissue. Our systematic studies of the nanoparticles penetration via this route confirmed this observation.[21]

To verify our MPM observations, we carried out high-resolution, high-sensitivity SEM/EDX measurements of ZnO nanoparticle penetration in the excised skin topically treated with ZnO-nano. Figure 6 shows the results of our observations. An SEM image shows a low-magnification morphological layout of the skin cross-section. In the central part of the image, a wedge-like skin fold converges inward. Several fragments of the bright-contrast debris are clearly localized in this skin fold. The EDX technique enables atomic species analysis locally. Integral x-ray spectra sampled at two sites of interest, SC/skin fold (solid circle) and epidermis (dashed circle) are shown in left-hand side panels Fig. 6. At least two prominent peaks of zinc (ZnK, ZnL, corresponding to excitation of the core electron shells in a zinc atom) and one oxygen peak were observed in the skin fold, as shown in panel EDX: stratum corneum. These are suggestive of the presence of ZnO in the skin fold, as expected considering the topical application of the sunscreen formulation on the skin. We note that ZnO-nano existed predominantly in an agglomerated phase. In contrast,

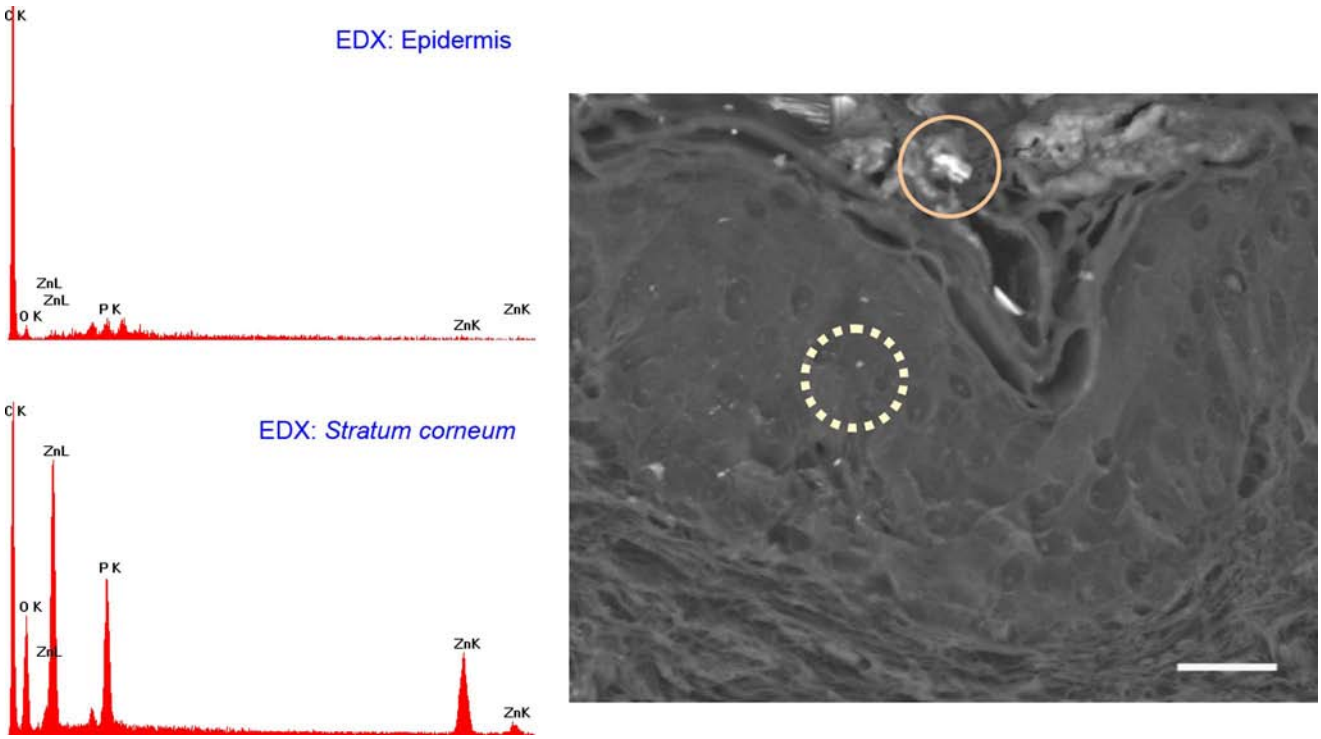

Fig. 6 SEM image (right-hand side panel) and EDX spectra (left-hand side panels) of the excised human skin topically treated with ZnO-nano. The EDX spectra sampled from the stratum corneum/skin fold (solid circle) and epidermis (dashed circle) areas are displayed in top (EDX: SC) and bottom (EDX: epidermis) left-hand side panels, respectively. Note EDX spectrum in SC shows two prominent peaks of atomic zinc origin (ZnL, ZnK). C, O, Zn, P, denote corresponding chemical elements. The ending letters K and L denote the characteristic binding energies of the core electron shells. Scale bar 20 μm.

no noticeable peaks were observed in the epidermis, as EDX-:epidermis panel shows. This result confirms our observation made by using multiphoton microscopy: ZnO-nano remained on the skin surface.

4 Discussion

The ZnO-nano nonlinear optical contrast on the cell autofluorescence background is remarkable and unexpected. This contrast could be due to several factors. First, the PL of ZnO nanoparticles is considerably enhanced compared to bulk ZnO. Guo et al.[22] have reported that the third-order nonlinear susceptibility $\chi^{(3)}_{\mathrm{ZnO}}$ of ZnO-nano sized $d=4$ nm is almost 500-fold of that of bulk ZnO. As this enhancement is likely to be due to quantum confinement effects, ZnO-nano, with a size of several tens of nanometers, exhibits quantum dot properties. The systematic study of $\chi^{(3)}_{\mathrm{ZnO}}$ versus ZnO-nano size in the size range of 6 to 18 nm has revealed a $\chi^{(3)}_{\mathrm{ZnO}}$ quadratic size dependence, with $\chi^{(3)}_{\mathrm{ZnO}}$ measured[23] to be 9.0×10^{-10} esu (expressed in cgs system of units) at $d=18$ nm and $\lambda=532$ nm. Second, ZnO-nano emission typically occurs in three major spectral bands centered at 385 nm (UV), 530 nm (green), and 590 nm (orange). The orange emission is broadband, and is due to oxygen interstitial defects, which disappear after high-temperature annealing in air.[19] Although the origin of the green broadband emission is not well understood, it is commonly believed to originate from oxygen vacancy defects. These defects may be situated on the surface of a ZnO-nano, and hence amenable to surface treatment by capping with polymer.[22] Further, as the surface capping resulted in considerable suppression of the broadband emission in green (accompanied by the UV emission enhancement) several other capping-free ZnO-nano synthetic routes yield similar results.[19,24] Our sample exhibited no detectable emission bands in the visible spectral range (see Fig. 1). As maintained in the literature, the narrowband UV emission at 385 nm is unlikely to be due to direct bandgap transition, as the Stokes shift between the absorption and emission bands is too large. It is hypothesized and corroborated experimentally that the UV emission is due to deep donors associated with oxygen vacancies. A PL-induced electron populates this vacancy followed immediately by its recombination with an available hole (exciton recombination) accompanied by a UV photon emission. These donors are localized and their population density in the nanocrystal is high, leading to dramatic enhancement of the quantum confinement effect and enhanced UV emission.

To evaluate attainable contrast of ZnO-nano on the autofluorescence background of skin, we compared the two-photon excitation fluorescence signal from ZnO-nano with that of the endogenous fluorophores typical to skin. The two-photon absorption cross-section of ZnO-nano, $\sigma^{(2\mathrm{ph})}_{\mathrm{ZnO}}$, which is governed by a third-order nonlinear process,[25] can be found by using the third-order nonlinear susceptibility, $\chi^{(3)}_{\mathrm{ZnO}}$ of ZnO reported in the literature[26]

$$\sigma_{\mathrm{ZnO}}^{(2\mathrm{ph})} = \frac{2\hbar\omega^2}{3Nn_0^2c^2\varepsilon_0}\,\mathrm{Im}\,\chi_{\mathrm{ZnO}}^{(3)}, \quad (1)$$

where $\hbar$ stands for the Plank's constant, $\omega = 2\pi c/\lambda$ is the optical angular frequency; N denotes nanoparticle concentration recalculated from the molar concentration of 10^{-4} M (reported in Ref. 22); n_0 is the refractive index of ZnO at $\lambda = 532$ nm, which amounts to 2.0; c is speed of light; $\varepsilon_0 = 8.854 \times 10^{-12}$ F/m is the dielectric permeability constant. We convert $\chi_{\mathrm{ZnO}}^{(3)}$ from 9.0×10^{-9} esu in the cgs system of units to $\chi_{\mathrm{ZnO}}^{(3)} \cong 1.3 \times 10^{-17}$ m^2/V^2 in the SI system of units. Substitution of these values to Eq. (1) yields

$$\sigma_{\mathrm{ZnO}}^{(2\mathrm{ph})} \cong 1.2 \times 10^{-49}\,\mathrm{m^4\,s/photon\ particle} \equiv 12\ \mathrm{GM}, \quad (2)$$

for an 18-nm ZnO particle at $\lambda = 532$ nm, where we used a convention of 1 GM $\equiv 10^{-50}$ m^4 s/photon molecule for two-photon absorption cross-section. To evaluate a fluorescent signal from our sample, it is important to determine the nanoparticle action cross-section $\sigma_{\mathrm{ZnO}}^{(\mathrm{TPEF})}$, which is defined as a product of the absorption cross-section and quantum yield Φ. Here Φ represents a number of fluorescence photons emitted per one absorbed photon (per two photons in TPEF). According to the literature reports,[27] the ZnO quantum yield varies depending on the crystal and surface quality, with a typical value of $\Phi = 0.02$. The two-photon action cross-section is evaluated to be $\sigma_{\mathrm{ZnO}}^{(\mathrm{TPEF})} = 0.26$ GM for an 18-nm particle typical for our experimental conditions. This value is much less compared to that of water-soluble Qdots, $\sim 5 \times 10^4$ GM (Ref. 10), and exogenous (externally introduced) fluorophores, such as fluorescein, ~50 GM. At the same time, $\sigma_{\mathrm{ZnO}}^{(\mathrm{TPEF})}$ is favorably comparable to that of the dominant skin endogenous fluorophores, including reduced NAD[P]H, FAD, and retinol, whose $\sigma_{\mathrm{fluo}}^{(\mathrm{TPEF})}$ does not exceed[28] 0.1 GM at 700 nm.

In the context of multiphoton imaging, the visibility of ZnO-nano material against the skin autofluorescence background is determined by its TPEF cross-section relative to that of endogenous fluorophores, its relative concentration, and its fluorescence emission spectral overlap with the dominant skin fluorophores. Skin autofluorescence has been investigated,[29] both *in vitro* and *in vivo*. The skin autofluorescence spectrum has been reported in the literature to feature three major component bands centered at 450, 520, and 625 nm on excitation in the wavelength range of 340 to 380 nm. The first two spectral bands corresponded to 75 and 25% of the total spectrum intensity, respectively.[15] These two peaks in the skin autofluorescence spectrum correspond to the fluorescence emission peaks of the endogenous skin fluorophores that include collagen, elastin, NAD[P]H, and FAD (Ref. 29), whereas the peak at 625 nm corresponds to porphyrins. Skin autofluorescence background, excited as a result of the nonlinear optical processes, is somewhat different. It is spectrally separated into an intense SHG signal from collagen, which occurs at a precisely half the laser excitation wavelength (UV range), a narrow emission band from 400 to 430 nm, and a broadband emission from 430 to 600 nm (see Fig. 1) (Ref. 14). In live skin, the autofluorescence spectrum in epidermis is dominated by NAD[P]H, as this coenzyme is involved in cellular energy metabolism. Vitamin derivatives, such as flavins, also have a noticeable contribution to the autofluorescence spectrum of epidermis *in vivo*. In the excised epidermis, the NAD[P]H contribution is markedly reduced due to degradation of the metabolic cycles, resulting in the reduced autofluorescence level and its spectral red-shift due to keratin and to some extent flavin components.

Note that the ZnO UV absorption band is advantageous to enable spectral discrimination of its emission signal from most endogenous fluorophores of skin, including NAD[P]H, riboflavin, folic acid, and retinol, all having emission bands in visible. At the same time, the emission band of pyridoxine falls[28] into that of ZnO, and demands attention in certain imaging scenarios. However, for the nanoparticle transdermal penetration study, confined to the SC and viable epidermis, such collagen-related molecules as pyridoxine, pose little problem, since they are predominantly present in dermis. The SHG signal from collagen [see Fig. 1(b)] did not present a problem due to its predominant location in the dermis. Further, this signal wavelength is precisely half the wavelength of the excitation source so that it may fall outside the ZnO PL spectral range. The ZnO-nano UV PL spectral band may overlap with that of the other endogenous fluorophores, leading to a degraded imaging contrast.

The femtosecond laser excitation wavelength of 740 nm used in our experiments is suboptimal for the excitation of ZnO TPEF, as the ZnO bandgap width of 3.4 eV ($\lambda = 350$ nm) requires two-photon excitation at a fundamental wavelength of 700 nm. At the same time, $\sigma_{\mathrm{ZnO}}^{(2\mathrm{ph})}$ dependence versus λ falls off gradually from 350 to 380 nm, whereas $\sigma_{\mathrm{ZnO}}^{(2\mathrm{ph})}$ ($\lambda = 740$ nm) $\cong 0.4\sigma_{\mathrm{ZnO}}^{(2\mathrm{ph})}$ ($\lambda = 700$ nm) (Ref. 23). At the same time, Iripman et al. have noted a steep increase of $\mathrm{Im}\,\chi_{\mathrm{ZnO}}^{(3)}$ versus the laser intensity.[23] Therefore, our evaluation of $\sigma_{\mathrm{ZnO}}^{(2\mathrm{ph})}$ [see Eq. (2)] must be treated as only a rough estimation. Note that, unlike in case of free excitons, characterized by $\sigma^{(2\mathrm{ph})} \propto d^3$, $\sigma_{\mathrm{ZnO}}^{(2\mathrm{ph})} \propto d^2$ in the size range $d = 6$ to 18 nm, revealing the bound exciton nature of ZnO-nano. Also $\sigma_{\mathrm{ZnO}}^{(2\mathrm{ph})}$ is sensitive to the crystal/surface quality. Our preliminary data on the nonlinear optical signal intensity versus input power suggests that three-photon nonlinear optical absorption makes a slight additional contribution to the excitation of ZnO-nano.[16] Although $\mathrm{Im}\,\chi_{\mathrm{ZnO}}^{(3)}$ has been recently measured, no data on the three-photon absorption cross-section of ZnO-nano has been reported to the best of our knowledge.

Application of the adapted multiphoton imaging system to imaging ZnO-nano enabled us to examine the existing hypothesis on the nanoparticle penetrability through the normal intact skin. Importantly, we have been able to investigate this question *in vivo* and show that the ZnO-nano did not penetrate human skin either *in vitro* or *in vivo*. This work is important, as it addresses the first aspect that may have caused ZnO-nano toxicity penetration. This work suggests that ZnO-nano, of about 15 to 30 nm in size, does not penetrate human skin. In contrast, the smaller molecules, such as salicylic acid (0.5 nm), do penetrate the skin.[30] This is consistent with a number of *in vitro* investigations of cosmetic-origin ZnO-nano penetration in skin that have been reported.[31,32] In our study, we used caprylic capric triglycerides formulation for ZnO-nano, which promotes passive diffusion of nanoparticles via a lipophilic intercellular pathway. This pathway represents the principle transdermal penetration route, and hence repre-

sents the most stringent test of the ZnO-nano penetrability, except for active skin enhancers. Electron micrographs of human skin show ZnO-nano mineral components are present on the surface of the skin and around desquaming corneocytes[17] and not in deeper tissues. Australia's Therapeutic Goods Agency has actively supported the notion that ZnO and TiO_2 remain on the surface of the skin and in the outer dead layer (SC) of the skin.[26]

The data contrasts the most recent results by Ryman-Rasmussen et al. that Qdots of the size range of 15 to 40 nm did penetrate porcine skin, long considered a reliable model of the human skin.[33] Three types of the Qdot nanoparticles with positive, neutral, and negative charges on the Qdot surface were found in epidermis and dermis passed the SC, followed the skin topical application *in vitro*. These Qdots were shown to cause a severe immunological cellular response, ultimately resulting in cell apoptosis.[34] The size range of our ZnO nanoparticles (15 to 30 nm) was commensurable with that reported by the authors. Based on our results[21] (also, to be communicated elsewhere), we argue that porcine skin represents a poor model of human skin in the context of transdermal penetrability to nanoparticles. Receptor phase penetration of zinc through the human epidermal membrane has been observed over 24 h using the Franz cell-based technique,[17] although it was likely to be negligible and in a form of hydrolyzed zinc ions rather than integral ZnO-nano.

In this context, it is unlikely that ZnO-nano would be toxic if skin penetration had occurred. Cytotoxicity, genotoxicity, and photogenotoxicity studies on TiO_2 or other insoluble nanoparticles should be interpreted with caution, since such toxicities may be secondary to phagocytosis of mammalian cells exposed to high concentrations of insoluble particles. Studies on wear debris particles from surgical implants and other toxicity studies on insoluble particles support the traditional toxicology view that the hazard of small particles is mainly defined by the intrinsic toxicity of particles, as distinct from their particle size. There is little evidence supporting the principle that smaller particles have greater effects on the skin or other tissues or produce novel toxicities relative to micro-sized materials. Overall, the current weight of evidence suggests that nano-materials such as nano-sized vesicles or ZnO and TiO_2 nanoparticles currently used in cosmetic preparations or sunscreens pose no risk to human skin or human health, although other nanoparticles may have properties that warrant safety evaluation on a case-by-case basis before human use.

5 Conclusion

We investigated *in vitro* and *in vivo* skin penetrability to nanoparticles of the size range typical to that used in cosmetic products, i.e., 15 to 30 nm. For the first time, the application of multiphoton microscopy has enabled imaging of both the wide bandgap nanostructures, e.g., ZnO-nano, and skin tissue/cellular architecture. ZnO appeared to have surprisingly high visibility against the skin autofluorescence background, which was attributed to its enhanced nonlinear two-photon action cross-section $[\sigma_{ZnO}^{(2ph)} \sim 0.26\ GM]$ favorably compared to that of the skin endogenous fluorophores, e.g., NAD[P]H and FAD; and "transparency window" of skin autofluorescence at 380 ± 20 nm occupied by the ZnO-nano principle photoluminescence. Nanoparticles have been found to stay on the SC, or fell into skin folds or hair follicle roots, thus, confirming safety of the ZnO-nano-based cosmetic products *in vivo*.

References

1. G. J. Nohynek, J. Lademann, C. Ribaud, and M. S. Roberts, "Grey goo on the skin? Nanotechnology, cosmetic and sunscreen safety," *Crit. Rev. Toxicol.* **37**(3), 251–277 (2007).
2. G. P. H. Dietz and M. Bahr, "Delivery of bioactive molecules into the cell: the Trojan horse approach," *Mol. Cell. Neurosci.* **27**(2), 85–131 (2004).
3. A. Beduneau, P. Saulnier, and J. P. Benoit, "Active targeting of brain tumors using nanocarriers," *Biomaterials* **28**(33), 4947–4967 (2007).
4. Z. P. Xu, Q. H. Zeng, G. Q. Lu, and A. B. Yu, "Inorganic nanoparticles as carriers for efficient cellular delivery," *Chem. Eng. Sci.* **61**(3), 1027–1040 (2006).
5. P. H. Youl, P. D. Baade, M. Janda, C. B. Del Mar, D. C. Whiteman, and J. F. Aitken, "Diagnosing skin cancer in primary care: how do mainstream general practitioners compare with primary care skin cancer clinic doctors?" *Med. J. Aust.* **187**(4), 215–220 (2007).
6. R. Alvarez-Roman, A. Naik, Y. Kalia, R. H. Guy, and H. Fessi, "Skin penetration and distribution of polymeric nanoparticles," *J. Controlled Release* **99**(1), 53–62 (2004).
7. K. F. Lin, H. M. Cheng, H. C. Hsu, L. J. Lin, and W. F. Hsieh, "Band gap variation of size-controlled ZnO quantum dots synthesized by sol-gel method," *Chem. Phys. Lett.* **409**(4–6), 208–211 (2005).
8. R. Dunford, A. Salinaro, L. Z. Cai, N. Serpone, S. Horikoshi, H. Hidaka, and J. Knowland, "Chemical oxidation and DNA damage catalysed by inorganic sunscreen ingredients," *FEBS Lett.* **418**(1–2), 87–90 (1997).
9. H. A. Jeng and J. Swanson, "Toxicity of metal oxide nanoparticles in mammalian cells," *J. Environ. Sci. Health, Part A: Toxic/Hazard. Subst. Environ. Eng.* **41**(12), 2699–2711 (2006).
10. D. R. Larson, W. R. Zipfel, R. M. Williams, S. W. Clark, M. P. Bruchez, F. W. Wise, and W. W. Webb, "Water-soluble quantum dots for multiphoton fluorescence imaging in vivo," *Science* **300**(5624), 1434–1436 (2003).
11. H.-Y. Lee, Y.-R. Chang, K. Chen, C.-C. Chang, D.-S. Tsai, C.-C. Fu, T.-S. Lim, Y.-K. Tzeng, C.-Y. Fang, C.-C. Han, H.-C. Chang, and W. Fann, "Mass production and dynamic imaging of fluorescent nanodiamonds," *Nat. Nanotechnol.* **3**, 284–288 (2008).
12. Z. F. Li and E. Ruckenstein, "Water-soluble poly(acrylic acid) grafted luminescent silicon nanoparticles and their use as fluorescent biological staining labels," *Nano Lett.* **4**(8), 1463–1467 (2004).
13. H. M. Cheng, K. F. Lin, H. C. Hsu, and W. F. Hsieh, "Size dependence of photoluminescence and resonant Raman scattering from ZnO quantum dots," *Appl. Phys. Lett.* **88**(26), 261909 (2006).
14. J. A. Palero, H. S. de Bruijn, A. V. van den Heuvel, H. Sterenborg, and H. C. Gerritsen, "Spectrally resolved multiphoton imaging of in vivo and excised mouse skin tissues," *Biophys. J.* **93**(3), 992–1007 (2007).
15. R. H. Na, I. M. Stender, L. X. Ma, and H. C. Wulf, "Autofluorescence spectrum of skin: component bands and body site variations," *Skin Res. Technol.* **6**(3), 112–117 (2000).
16. D. C. Dai, S. J. Xu, S. L. Shi, M. H. Xie, and C. M. Che, "Efficient multiphoton-absorption-induced luminescence in single-crystalline ZnO at room temperature," *Opt. Lett.* **30**(24), 3377–3379 (2005).
17. S. E. Cross, B. Innes, M. S. Roberts, T. Tsuzuki, T. A. Robertson, and P. McCormick, "Human skin penetration of sunscreen nanoparticles: in-vitro assessment of a novel micronized zinc oxide formulation," *Skin Pharmacol. Appl. Skin Physiol.* **20**(3), 148–154 (2007).
18. K. Konig, A. Ehlers, F. Stracke, and I. Riemann, "In vivo drug screening in human skin using femtosecond laser multiphoton tomography," *Skin Pharmacol. Appl. Skin Physiol.* **19**(2), 78–88 (2006).
19. H. M. Cheng, H. C. Hsu, S. L. Chen, W. T. Wu, C. C. Kao, L. J. Lin, and W. F. Hsieh, "Efficient UV photoluminescence from monodispersed secondary ZnO colloidal spheres synthesized by sol-gel method," *J. Cryst. Growth* **277**(1–4), 192–199 (2005).
20. V. Tuchin, *Tissue Optics: Light Scattering Methods and Instruments for Medical Diagnosis*, Kluwer Academic Publishers, Boston (2000).
21. A. J. X. Zhao, J. A. Ross, M. Sarkar, W. Sanchez, A. V. Zvyagin, and M. S. Roberts, "Nanoparticles penetration through human skin, much ado about nothing?", presented at the Trailblazing the Skin Frontier: Evidence Base, Opportunities&Training, George Washington Univer-

sity, Washington, DC, 11–13 August 2007 (2007), pp. 22.
22. L. Guo, S. H. Yang, C. L. Yang, P. Yu, J. N. Wang, W. K. Ge, and G. K. L. Wong, "Highly monodisperse polymer-capped ZnO nanoparticles: preparation and optical properties," *Appl. Phys. Lett.* **76**(20), 2901–2903 (2000).
23. L. Irimpan, V. P. N. Nampoori, P. Radhakrishnan, B. Krishnan, and A. Deepthy, "Size-dependent enhancement of nonlinear optical properties in nanocolloids of ZnO," *J. Appl. Phys.* **103**(3), 033105 (2008).
24. M. M. Demir, R. Munoz-Espi, I. Lieberwirth, and G. Wagner, "Precipitation of monodisperse ZnO nanocrystals via acid-catalyzed esterification of zinc acetate," *J. Mater. Chem.* **16**(28), 2940–2947 (2006).
25. R. L. Sutherland, *Handbook of Nonlinear Optics*, Marcel Dekker, New York (1996).
26. "A review of the scientific literature on the safety of nanoparticulate titanium dioxide or zinc oxide in sunscreens", edited by A. Therapeutic Goods Administration (Australian Government, Department of Health and Aging, 2006).
27. M. Schubnell, I. Kamber, and P. Beaud, "Photochemistry at high temperatures—potential of ZnO as a high temperature photocatalyst," *Appl. Phys. A: Mater. Sci. Process.* **64**(1), 109–113 (1997).
28. W. R. Zipfel, R. M. Williams, R. Christie, A. Y. Nikitin, B. T. Hyman, and W. W. Webb, "Live tissue intrinsic emission microscopy using multiphoton-excited native fluorescence and second harmonic generation," *Proc. Natl. Acad. Sci. U.S.A.* **100**(12), 7075–7080 (2003).
29. N. Kollias, R. Gillies, M. Moran, I. E. Kochevar, and R. R. Anderson, "Endogenous skin fluorescence includes bands that may serve as quantitative markers of aging and photoaging," *J. Invest. Dermatol.* **111**(5), 776–780 (1998).
30. K. Harada, T. Murakami, E. Kawasaki, Y. Higashi, S. Yamamoto, and N. Yata, "Invitro permeability to salicylic-acid of human, rodent, and shed snake skin," *J. Pharm. Pharmacol.* **45**(5), 414–418 (1993).
31. Z. S. Kertesz and A. Z. Kiss, "Quality of skin as a barrier to ultra-fine particles," Contribution of the IBA Group to the Nanoderm EU-5 Project (2003–2004).
32. C. G. J. Hayden, S. E. Cross, C. Anderson et al., "Sunscreen penetration of human skin and related keratinocyte toxicity after topical application," *Skin Pharmacol. Appl. Skin Physiol.* **18**(4), 170–174 (2005).
33. J. P. Ryman-Rasmussen, J. E. Riviere, and N. A. Monteiro-Riviere, "Penetration of intact skin by quantum dots with diverse physicochemical properties," *Toxicol. Sci.* **91**(1), 159–165 (2006).
34. J. P. Ryman-Rasmussen, J. E. Riviere, and N. A. Monteiro-Riviere, "Surface coatings determine cytotoxicity and irritation potential of quantum dot nanoparticles in epidermal keratinocytes," *J. Invest. Dermatol.* **127**(1), 143–153 (2007).

J. Biophoton. **1**, No. 6, 478–493 (2008) / **DOI** 10.1002/jbio.200810058

Journal of BIOPHOTONICS

FULL ARTICLE

In vitro and *in vivo* imaging of xenobiotic transport in human skin and in the rat liver**

Michael S. Roberts[1,*], *Matthew J. Roberts*[1], *Thomas A. Robertson*[1], *Washington Sanchez*[1], *Camilla Thörling*[1], *Yuhong Zou*[1], *Xin Zhao*[2], *Wolfgang Becker*[3], *and Andrei V. Zvyagin*[2]

[1] Therapeutics Research Unit, Department of Medicine, University of Queensland, Princess Alexandra Hospital, Woolloongabba, QLD 4102, Australia
[2] Physics, Macquarie University, Sydney, NSW 2109, Australia
[3] Becker & Hickl GmbH, Nahmitzer Damm 30, 12277 Berlin, Germany

Received 19 September 2008, revised 24 October 2008, accepted 27 October 2008
Published online 24 November 2008

Key words: Multi-photon tomography, fluorescence lifetime imaging, pharmacokinetics, zinc oxide nanoparticle, fluorescein

Multiphoton tomography was used to examine xenobiotic transport *in vivo*. We used the photochemical properties of zinc oxide and fluorescein and multiphoton tomography to study their transport in the skin and in the rat liver *in vivo*. Zinc oxide nanoparticles were visualised in human skin using the photoluminescence properties of zinc oxide and either a selective emission wavelength band pass filter or a filter with fluorescence lifetime imaging (FLIM). Zinc oxide nanoparticles (30 nm) did not penetrate into human skin *in vitro* and *in vivo* and this was validated by scanning electron microscopy with X-ray photoelectron spectroscopy. Fluorescein was measured in the liver using FLIM. Fluorescein is rapidly extracted from the blood into the liver cells and then transported into the bile. It is suggested that multiphoton tomography may be of particular use in defining *in vivo* 4D (in both space and time) pharmacokinetics.

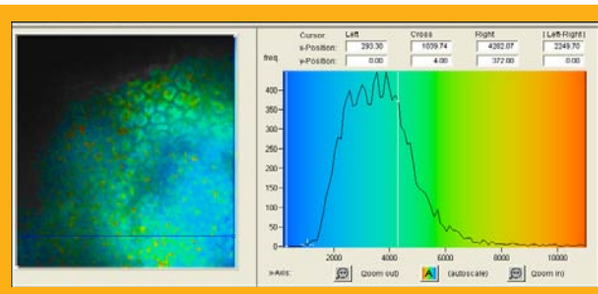

FLIM of ZnO *in vivo* in skin

1. Introduction

The liver and the skin are the two organs in the body that can spontaneously regenerate. Much of our work in pharmacokinetics is limited by the necessity to deduce events that occur in organs, such as the skin and the liver, from outflow profiles seen in the blood or perfusate after administration of compounds of interest [1, 2]. The mathematical shape of the profile is then used together with a model based on the underlying organ anatomy and physiology to define events that occur within that organ. A limitation in this analysis is the assumption of a "black box" model and the necessity to present the disposition kinetics (pharmacokinetics) of the solute in a simple form, usually in one dimension over time. This work may then be used, for instance, to examine the role of chemical structure of solutes on their

* Corresponding author: e-mail: m.roberts@uq.edu.au, Phone: +61732402546 Fax: +61732405806
** Abstracted from a lecture presented at FLIM2008, Saarbrucken, Germany, June 2008

transport kinetics, the impact of disease on transport and the role of the delivery system in releasing a solute into the blood. However, such analysis does not allow a clear understanding of the spatial processes involved. As a consequence, debate has existed in terms of, for instance, should the liver be regarded as behaving like a tube or like a well-stirred compartment in predicting the effects of changing blood flow, metabolising enzyme and transporter activity and protein binding on drug clearance [3]. A more realistic model, based on impulse – response and histochemical spatial data is the dispersion model [4]. However, this model is limited in being able to describe the interrelationship between axial and radial zonation of uptake processes and the resultant pharmacokinetics. A similar problem exists with the skin in that a key target site for drug action is the viable epidermis but relatively little is known about the gradients of chemicals in the viable epidermis at different times following topical applications.

The ability to visualise solute concentrations in time and in space within organs (4D imaging) would enable the spatial pharmacokinetics to be better defined. In principle, this is not a new concept as *in vivo* microscopy has been around for a very long time. As Ellinger pointed out in 1940, the term intravital microscopy describes the use of a fluorescence microscope to observe processes in the living organism [5]. Ellinger went on further to suggest that this is "a method, which has opened up a new field of research, as it permits the observation of biological processes occurring within living organs and cells by extending the two dimensional pictures of the usual microscopy space into three dimensional space and adding the fourth dimension of time…" [5]. One illustration of the technique is the *in vivo* studies on fluorescein transport in the liver by Hanzon in 1952, which we found provided an excellent foundation for the multiphoton tomography studies in the liver described here [6]. Today, intravital fluorescence microscopy is mainly associated with imaging the microcirculation in organs [7].

Multiphoton tomography has, over the last 20 years, developed into a technique that enables the simultaneous monitoring of both the morphology of an organ and solute transport in that organ. It has been used in the skin [8, 9], the liver [10] and other organs [11, 12]. It is also being increasingly used in clinical applications [13].

In this paper, we report on the application of multiphoton tomography to examine the transport of nanoparticles in the skin and fluorescein molecules in the liver *in vivo*. Two key techniques were applied to enable differentiation from the autofluorescence present in the organ: a selective fluorescence filtering and FLIM analysis. Zinc oxide nanoparticles (ZnO-nano) were chosen as they are now widely used in sunscreen products in a nanosize range in order to provide transparency [14] but concerns remain about their safety (SCCP, Statement on Zinc oxide used in sunscreens, SCCP/0932/05 Adopted on 20 September 2005). Nanoparticles with a similar size to the reported ZnO nanoparticles have been shown to penetrate the deeper layers of pig skin [15].

2. Methods

2.1 DermaInspect / Multiphoton FLIM

Multiphoton tomography was performed with a DermaInspect system (JenLab GmbH, Jena, Germany), illuminated with an ultra short (85 femtosecond pulse width) pulsed mode-locked 80-MHz Titanium: Sapphire MaiTai laser (Spectra Physics, Mountain View, USA), with a tuning range of 710–920 nm. A TCSPC (time correlated single photon counting) 830 detector (Becker & Hickl, Berlin, Germany) was integrated into the tomography system to enable FLIM measurements. FLIM analysis of ZnO skin penetration was undertaken using SPC 830 2.9 on a dual core computer using a Windows XP platform. The module builds up a photon distribution over the scan coordinates, x and y, and the time in the fluorescence decay, t [16]. Signals from four photon counting detectors working in different wavelength intervals are processed simultaneously. Fluorescence lifetime analysis was done by the SPCImage data analysis package of Becker & Hickl. The software uses iterative convolution with a single, double, or triple-exponential model to determine the decay parameters in the individual pixels of the scan. A description of the data analysis can be found in [17]. In most studies, the photon decay profiles were analysed with a multicomponent exponential fit so as to obtain the best possible chi-squared (χ_i^2) value and at the same time measure both key viable epidermal and ZnO lifetime signals. A HF110 filter wheel (Prior) was used to switch between the following emission filters: BG39 (350–650 nm), FDIG (500–580 nm) and FDIB (320–520 nm). The objective lenses were Plan-Neofluar oil-immersion 40×/1.30 or C-Apochromat 10×/0.45 W (Carl Zeiss, Germany) as indicated. The space between the in vivo adaptor and the objective lens was filled with index-matching oil and 37% sucrose for the high- (40×) and low (10×) magnification objectives, respectively.

Multiphoton imaging involved tightly focusing ultra short pulsed excitation laser light onto a sample (JenLab GmbH Schillerstraße 107745 Jena Germany) by using a high-NA oil-immersion microscope

Journal of
BIOPHOTONICS

objective (40×, NA 1.3). The very high instantaneous intensity in the femto-litre focal volume elicited a material nonlinear optical response, with two-photon excited fluorescence (TPEF) being one manifestation of the nonlinear process. The fluorescence origin is localized exclusively in the focal volume resulting in the "optical sectioning" property of multiphoton tomography [18]. The thickness of the optical section is determined by the axial transfer function of the optical multiphoton imaging system, which was measured to be 2 μm for our experimental configuration. The excitation light represented a pulsed femtosecond laser, which was a tuneable, computer-controlled titanium-sapphire laser (MaiTai, Spectra Physics) whose wavelength was fixed to 740 nm for all skin experiments. A laser pulse width and repetition rate was 85 femto-seconds and 80 Megahertz, respectively. The incident optical power was set to 12 mW in stratum corneum and epidermis. A focused laser spot was rastered across the sample using two galvanometer mirrors. The excited fluorescence was collected by the same imaging optics and reflected to a detection arm by a dichroic mirror that was transparent for the excitation radiation in the IR spectral range, and reflective for UV and visible. In the detection arm, the fluorescence was split between two detection paths, termed main detection path, and FLIM detection path. Both detection paths included a filter wheel which contained a broadband spectral filter, e.g. BG39, whose main function was blocking the IR excitation light, so that most spectral content of the tissue auto fluorescence was captured. The FLIM path detectors comprised four channels terminated by four fast-response optical detectors, photomultiplier tubes, suitable for capturing single-photon events for fluorescence lifetime analysis. The four detection channels were equipped with pre-selected spectral filters: with band pass of 350 nm–450 nm (Channel 1); 450 nm–515 nm (Channel 2); 515 nm–620 nm (Channel 3); 620 nm–670 nm (Channel 4). An image was formed by recording detector signals versus the focal spot position in the sample. Two images from the two channels could be overlaid at a post processing stage. In order to optimize spectral filter configuration in the detection arms, we carried out a preliminary imaging experiment using two samples, as detailed elsewhere [19].

2.2 Zinc oxide nanoparticles

ZincClear CCT-60 (60% w/w) (Advanced Nanotechnology Ltd., WA, Australia) comprised ZnO particles sized 26–30 nm coated with polymethylsilsesquioxane suspended in caprylic/capric triglycerides [14] were used in all human skin penetration studies described here. These nanoparticles were fabricated by using the mechanochemical processing technology based on dry milling that induced chemical reactions through ball-powder collisions resulting in nanoparticle formation within a salt matrix. Particle size was defined by the chemistry of the reactant mix, milling and heat treatment conditions. We have presented a transmission electron microscope (TEM) picture of these coated ZnO particles, their photon correlation spectroscopy (PCS) size distribution of the micronized ZnO particles and their spectral transmittance of ZnO particles in aqueous solution previously [14].

2.3 Zinc oxide photoluminescence (PL) lifetime

The emission signal decay of uncoated and coated ZnO-nano was studied using 405 nm picosecond laser excitation. As it is known that ZnO photoluminescence is characterised by complex spectral and photoluminescence lifetimes, this data were acquired with a BH DCS-120 confocal scanning FLIM system. The TCSPC module was an SPC-830. A BH DPC-120 module was employed in the multiscaler imaging mode and excitation pulses of several 100 ps duration (BDL-405SMC laser). A pulse period of about 100 μs was controlled by a pulse generator selected to resolve slow decay components of the zinc oxide that was characterized by decay times of hundreds of nanoseconds. The pulses were synchronized with the pixel clock of the scanner. For FLIM measurements a SPC-830 TCSPC (time-correlated single photon counting) FLIM module was integrated into the tomography system. The module builds up a photon distribution over the scan coordinates, x and y, and the time in the fluorescence decay, t [16]. Signals from four photon counting detectors working in different wavelength intervals are processed simultaneously. Fluorescence lifetime analysis was done by the SPCImage data analysis package of Becker & Hickl. The software uses iterative convolution with a single, double, or triple-exponential model to determine the decay parameters in the individual pixels of the scan. A description of the data analysis can be found in [17].

2.4 Skin studies

Approximately 0.1 g of ZincClear CCT-60 was applied evenly to the selected area (0.8–1.2 cm^2) of the human subjects and rubbed in for 5 minutes on the forearm, after pre-cleaning the skin with ethanol. The small amount was chosen arbitrarily to repre-

sent normal application conditions by users. The area of application was small in comparison with normal application of sunscreens for sun blocking purposes. Subsequently, the treated area was non-invasively imaged using the multiphoton imaging system. The skin surface of study was covered with a 17-μm-thick microscope glass cover slip to ensure aberration-free imaging.

Images were acquired in two sessions: (I) before application (control), (II) 4 hr after the topical application, following washing of the excess from the skin surface. After Session I, the subject was allowed to move, as per usual daily routine. Session II was carried out following removal of excess ZnO with wet paper towel, where the ZnO dispersion formulation residue was washed away from the superficial layers of the skin. The rationale behind the times at which the images were recorded is as follows. Imaging immediately before application serves as control to time-lapse imaging. Imaging after four hours was chosen as a representative of outdoor activities of the native population of South East of Qld. All experiments conducted on human subjects were done with approval of the Princess Alexandra Hospital Research Committee (Approval no. 097/090, administrated by the University of Queensland Human Ethics Committee) and subjects gave their written consent. Excised abdominal human skin obtained after elective plastic surgery was used in *in vitro* studies.

2.5 Scanning Electron Microscope (SEM) and X-ray photoelectron spectroscopy (EDX)

We employed a Philips XL30 FEG scanning electron microscope, with a backscattered electron detector, an integrated EDX energy-dispersive X-ray microanalysis system. The following procedure was used for sample preparation for SEM/EDX imaging and microanalysis. ZnO nanoparticle formulation was applied on the skin sample, and incubated for 2–24 hours. Several skin patches were tape-stripped 10–20 times on the areas of interest, whilst the other patches remained pristine. These nanoparticle-treated skin samples were fixed in 2.5% glutaraldehyde solution, a requirement of the SEM facilities and workplace health and safety protocols, prior to freeze drying. Before imaging, all the samples were vacuum-coated with 20–50 nm carbon coating. Conductive paint was applied to the aluminium stub holder. The fixed skin was cut into small cubical shaped blocks approximately 1 cm^3, followed by snap freezing with a specially made copper press that had been dipped in liquid nitrogen for 5 minutes. Whilst in the press, the samples were further dipped in liquid nitrogen and then freeze dried. The small freeze dried skin samples were mounted on the SEM and imaged.

The SEM was operated at 15–20 kilovolts acceleration voltage and high vacuum therefore all organic tissue needs to be fixed and dried. Images were obtained under 11.3 mm working distance (the distance between lens and the sample stage). The aperture and probe current settings were 3 and 7, respectively. The focus, brightness, and contrast were adjusted for each image.

2.6 Rat liver studies

In brief, the surgery to enable the multiphoton tomography imaging of the liver followed the general approach described by Hanzon [6] for intravital fluorescein microscopy. Male Wistar rats (weighing approximately 300 g) were anesthetized by intraperitoneal injection of xylazine (10 mg/kg) and ketamine hydrochloride (90 mg/kg) followed by a repeat administration of xylazine (2.45 mg/kg) and ketamine (22 mg/kg) intraperitoneally 90 min after the initial dose and then every 40 minutes thereafter. The femoral vein was cannulated and used to dose the rat with heparin (1 mg/100 g). A laparotomy was then performed with the rat falciform ligament and ensiform process between liver and diaphragm cut to reduce vibration of the liver associated with respiration. The bile duct was cannulated and the right lateral liver lobe placed on top of moist gauze covered support. After 20 min, multiphoton images of the liver were taken with fluorescein (5% in PBS, 400 μL/kg body weight) being administered through the femoral vein at different times. In a typical imaging experiment, the rat liver surface was brought to the focal plane of the objective lens. The laser power was then set to a power of $P = 10-15$ mW at a mean wavelength of 750 nm to excite a sufficient autofluorescence signal, with the BG39 emission filter in the main detection pass (the filter blocks the 750 nm excitation light). Fluorescein was observed by excitation with $P = 15-25$ mW at 920 nm with the FDIG emission filter in the detection path. FLIM Channels 2 and 3 were supposed to capture the full spectral content of the fluorescein fluorescence signal. We employed channel 2 for the fluorescence signal acquisition, display and analysis because the channel 3 signal intensity and distribution was much weaker than for channel 2.

Rat bile isolated 20 minutes after injection of fluorescein was separated by HPLC into fractions containing fluorescein and fluorescein glucuronide.

All animal studies confirmed with the approval from the University of Queensland, ethics number 088/88/NHMRC.

Journal of
BIOPHOTONICS

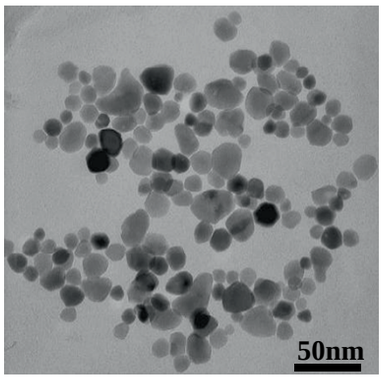

a)

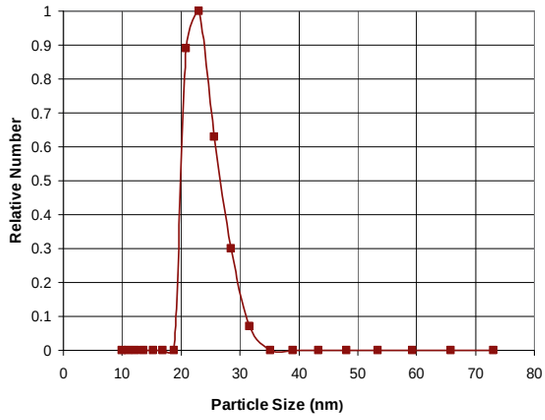

b)

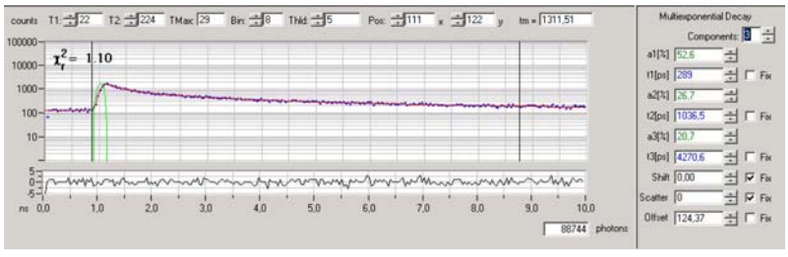

c)

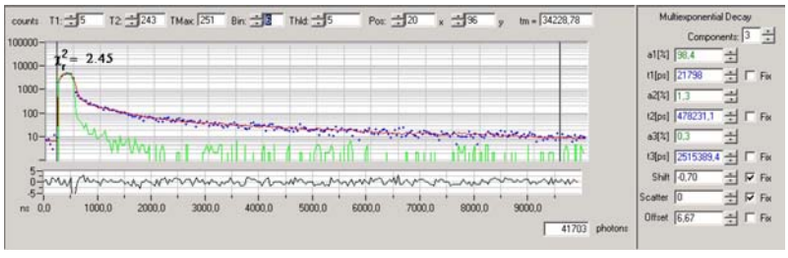

d)

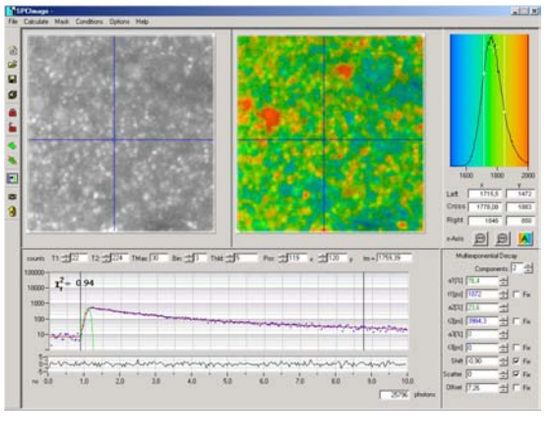

e)

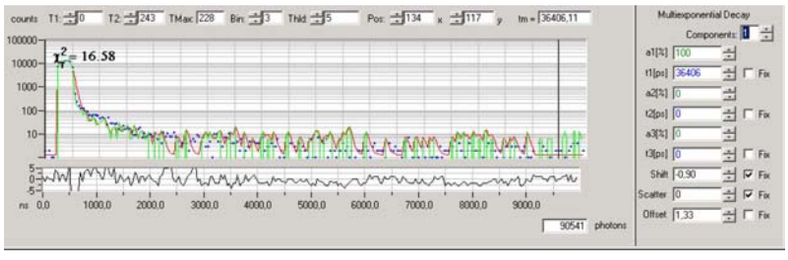

f)

Figure 1 (online colour at: www.biophotonics-journal.org)
a) TEM and b) PCS size distribution of coated ZnO nanoparticles [14]; c) Fluorescence decay of uncoated ZnO-nano measured with a bh DCS-120 confocal scanning FLIM system and a SPC-830 TCSPC module and d) Slow luminescence decay phenomena for uncoated ZnO recorded with a bh DPC-120 module in the multiscaler imaging mode with excitation pulses of a few 100 ns duration and a pulse period of about 100 µs generated by a BDL-405SMC laser in the CW mode, controlled by a pulse generator. The pulses were synchronised with the pixel clock of the scanner. The green curve is the IRF measured at a fluorescence-free ceramics target, the blue curve is luminescence decay and the red curve is the multicomponent fit. e) Fluorescence decay of coated ZnO-nano measured at short times and f) Lack of slow luminescence decay phenomena for coated ZnO.

3. Results

3.1 ZnO characterisation and FLIM characteristics

The coated ZnO nano used in these studies are aggregates that exist as separate entities 20–30 nm in diameter (Figure 1a and 1b). The fluorescence decay for uncoated ZnO-nano at 405 nm excitation wavelength is multi-exponential, with components of 289 ps, 1.036 ns, and 4.27 ns (Figure 1c) and there is a large offset in the signal due to the presence of extremely slow decay components. The 289 ps fluorescence lifetime is dominant for zinc oxide nano, with other short time components with lifetimes of 1.04 ns, and 4.27 ns only contributing about 1% of the total signal. The 289 ps lifetime was therefore used in later FLIM analyses. Figure 1d shows the resolved slow decay components. A nonlinear regression fit indicates that decay components of 21 ns, 478 ns, and 2.5 μs exist for ZnO-nano. In contrast to the uncoated ZnO, ZnO-nano coated with polymethylsilsesquioxane exhibited only short fluorescence components (Figure 1e). As is evident in Figure 1 f, the measured μs luminescence waveform with the DPC-230 is identical with the IRF indicating that the coating had suppressed the longer luminescence decay times. It was unclear from our work whether ZnO had a SHG component. It was expected to show up as an extremely fast decay component in the lifetime analysis. However, it is likely that our signal is 2-photon induced photoluminescence (TFPL), and not SHG because: (1) the band pass filter has FWHM of 20 nm and centred at 380 that will attenuate SHG signal that is located at the border of the filter transmission. The SHG signal width is of smaller width that the fundamental signal at 740 nm that is assumed roughly 10 nm, as it is translated into the high-frequency spectral domain. In addition, we would have noticed significant modulation of our ZnO-signal versus several nm detuning from 740 nm. The signal should be much more tolerant to the detuning in case of TFPL, as it is characterised by the broader line width; (2) the signal persisted when the laser was tuned to about 800 nm and (3) although the ZnO crystal can support SHG due to its non-centrosymmetric structure, as its dielectric susceptibility is much reduced in the nanometre range, its small crystal size does not favour SHG. It is recognised that collagen represents an efficient material for SHG due to its large dielectric susceptibility and non-centrosymmetric structures of almost sub-micron in diameter, and which is probably extended in many tens of microns in the axial direction. Our studies were limited to the epidermis and not the dermis, where collagen is located.

3.2 Skin studies

About 60 individuals of different age, race and sex have been imaged to date. The data shown in Figure 2a are representative of the range of participants studied, here including a female Asian aged 25–30 years, a male Indian aged 45–50 and a Caucasian aged 35–45. A comparison of the emission spectra for coated ZnO-nano and epidermis is shown in Figure 2a. It is evident that a filter band pass, BP380, centre wavelength 380 nm, FWHM 20 nm enables the selective measurement of coated ZnO-nano without endogenous fluorescence interference.

Figure 2b shows band pass measured of zinc oxide penetration after application of the coated ZnO-nano into forearm human skin *in vivo*. The coated ZnO-nano is only found within the grooves (also called skin folds and dermaglyphs) in the topmost layer of stratum corneum after 4 hours of application. No penetration of coated ZnO-nano into the viable epidermal cells was observed. The *in vivo* imaging experiments of human skin also suggest that the lack of the coated ZnO-nano formulation's penetration into forearm skin after 4 hours is common to subjects with varying racial characteristics. The fluorescence intensity of zinc oxide in the band pass (arbitrary units 68 ± 12 SD, $n = 6$) was significantly more (>10fold and $p < 0.0001$, *t*-test)) that of the background skin in the band pass (arbitrary units 4 ± 0.17 SD, $n = 6$).

The fact that no coated zinc oxide penetration occurred into epidermal cells was verified using SEM and EDX (Figure 2c). Using SEM imaging also confirms that ZnO-nano (as evident by the presence of peaks for zinc in EDX) are only localised in skin folds (Figure 2b). Other regions of the epidermis do not have any zinc oxide present as evident by the lack of peaks in EDX. The intensity of zinc peaks in the regions where zinc were present (arbitrary units 70 ± 21 SD, $n = 6$) was significantly more (>10 fold and $p > 0.0001$, *t*-test) than that of the background skin in the band pass (arbitrary units 4 ± 1 SD, $n = 6$). Independent studies, using platinum coating of coated ZnO-nano and SEM imaging confirmed that the mean size of the ZnO-nano on the skin surface was ~30 nm.

Figures 3 and 4 are representative pictures of ZnO nano penetration into the skin of a Caucasian male aged 40–50 years. Figure 3a–c show results obtained for in the stratum corneum *in vivo* (at 10 μm depth) in control skin specimens (ZnO absent) whereas Figs. 3d–f are the results when ZnO is present using band pass fluorescence and FLIM techniques. It is apparent there is superficial penetration of zinc oxide into outermost layers of the stratum corneum *in vivo* in Figure 3. The presence of ZnO in the same specific, limited areas is evident for the

Journal of
BIOPHOTONICS

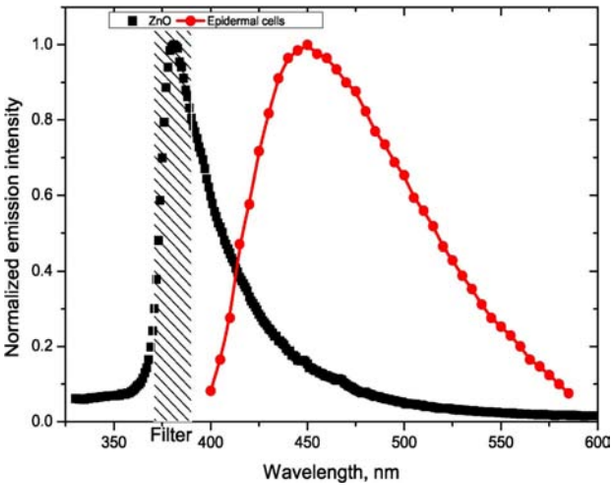

a)

Figure 2 (online colour at: www.biophotonics-journal.org) a) Emission spectra for zinc oxide and epidermal cells from an excitation wavelength of 740 nm. A band-pass filter BP380 was used to discriminate the zinc oxide photoluminescence signal from the skin autofluorescence; b) Overlaid multiphoton images of human skin *in vivo* (colour-coded green) and ZnO-nano distribution (colour-coded red) 4 hours after its topical application to the forearm for different racial skin types. The ZnO-nano distribution in red and human skin in green (top – Asian female; middle – Caucasian male; bottom – Indian male) with measurements in the stratum corneum (SC) and viable epidermis (Epidermis) with the times after application shown – the zinc oxide was washed off at 8 hours and imaged after 24 hours. Depth of viable epidermis visualised was 35 μm; c) Scanning electron microscopy with EDX imaging of ZnO-nano distribution into different areas of *in vitro* human epidermis.

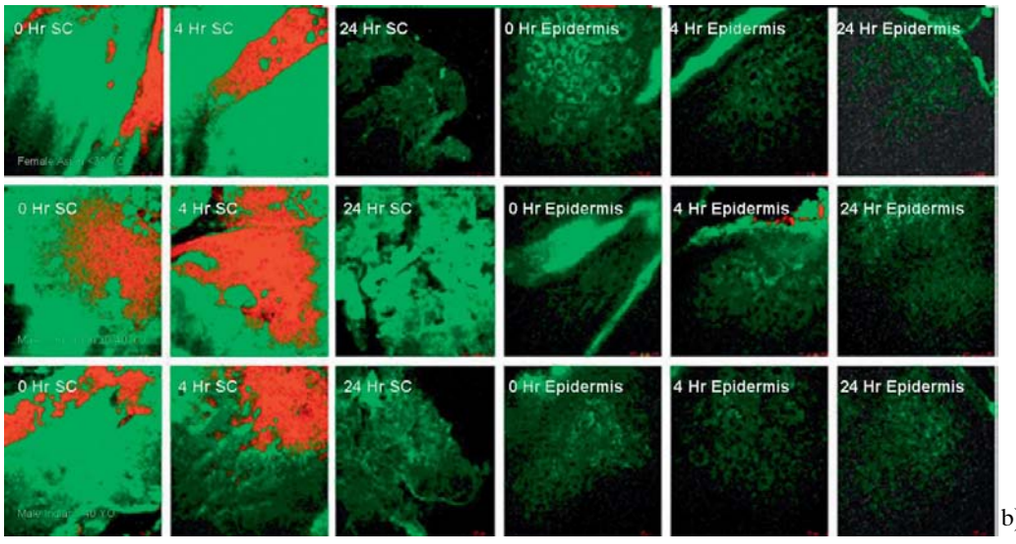

b)

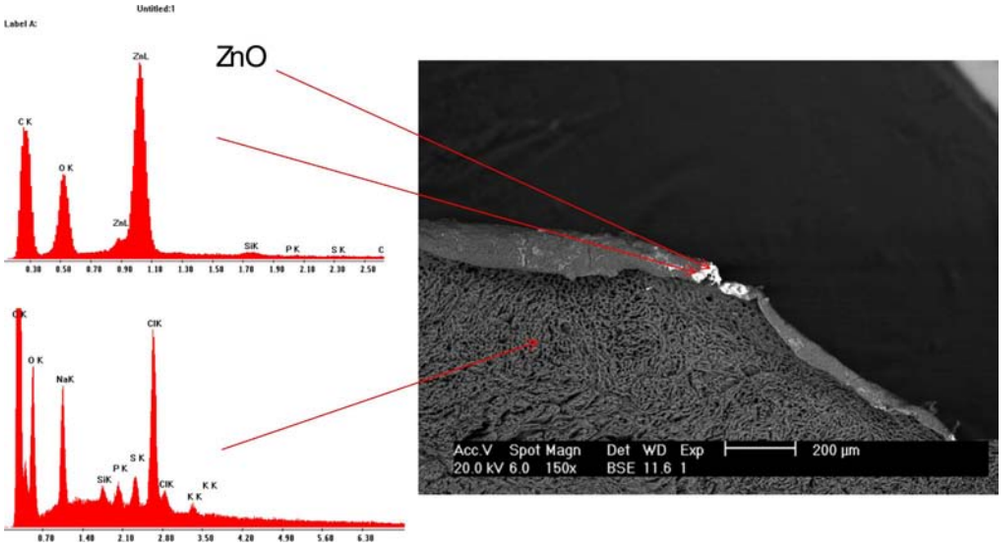

c)

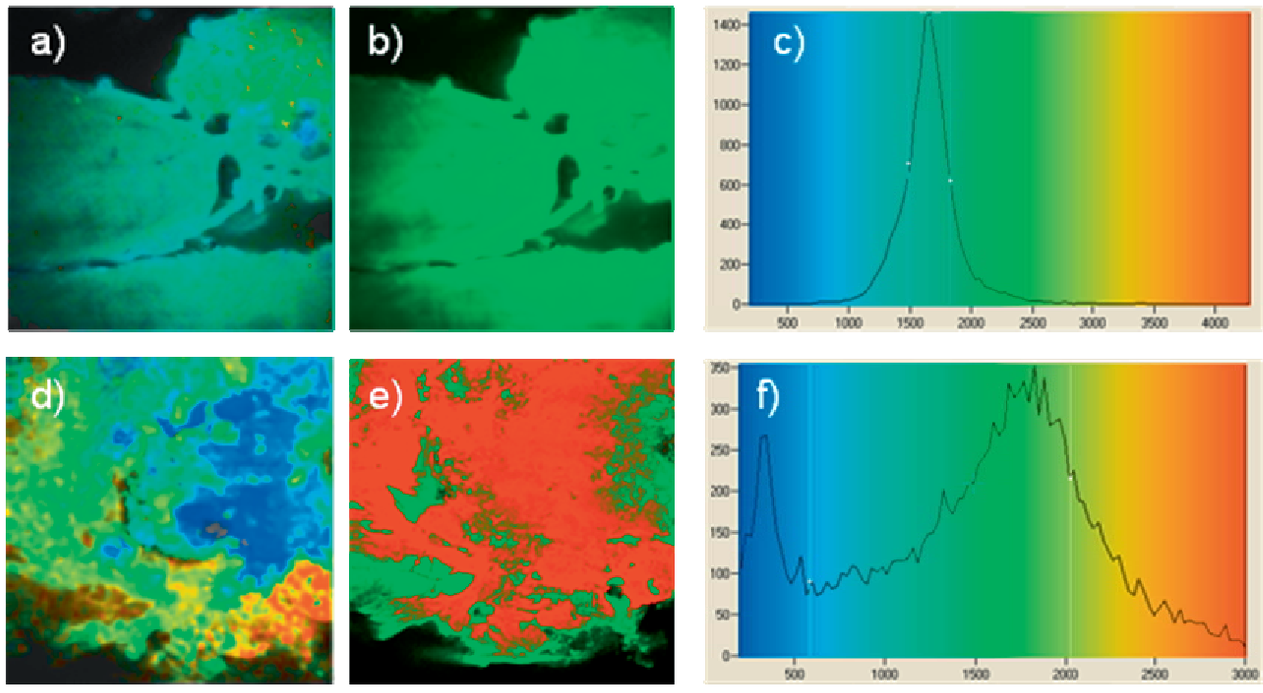

Figure 3 (online colour at: www.biophotonics-journal.org) *In vivo* control (a–c) and ZnO CCT-60 treated skin after 4 hours application (d–f), 10 μm from the surface. a) FLIM false colour (350–450 nm); b) live image single PMT overlay of BG39, (350–650 nm), green, and BP380, short band pass, red. c) Shows the histogram result from the FLIM analysis with a peak at 1800 ps, corresponding to endogenous fluorescence with emission 350–450 nm. d) FLIM false colour (350–450 nm) in treated skin; e) live image single PMT overlay of BG39, (350–650 nm), green, and BP380, short band pass, red; and f) Shows the histogram result from the FLIM analysis with peaks, corresponding to ZnO lifetime in the stratum corneum *in vivo*, are showing between 300 and 1800 ps.

FLIM images (Figure 3d), the band pass multiphoton tomography (Figure 3e) and corresponds to the short photoluminescence lifetime for ZnO at ~289 ps. The band pass data appears to appropriately show ZnO spread across the surface at 10 μm depth of skin. Interpretation of the FLIM results is more difficult as there are undefined interactions owing between ZnO and the skin, which are presently being studied further.

In an attempt to study FLIM for ZnO nanoparticles, the skin was treated with ZnO (CCT60) for 4 hours after which the skin was visualised with multiphoton tomography at a range of depths below the skin surface and compared to untreated skin (Figure 4). At 10 μm from the surface there is an additional peak at 270 ps, which cannot be seen in the control. This represents the short lifetime of ZnO, which is the dark blue colour in the false coloured image (Figure 4a–b). At 31 μm, a peak at about 3000 ps is apparent in the treated skin but not in the control (Figure 4b–c). However, in viable epidermis, 45 μm from the surface, no ZnO was found in the treated skin, because in comparing the histograms in the control and treated skin, they appear to be similar. This indicates that no ZnO nanoparticles has penetrated into the viable epidermis (Figure 4e–f).

3.3 *Liver studies*

Figure 5a shows a reference image reported by Hanzon [6] in 1952 for the intravital fluorescence microscopy for rat liver *in vivo*. He suggested that "yellow white fluorescent granules" in the Kuppfer cells [6] (we believe that these are more likely to be stellate cells) dominate the autofluorescence seen in the liver after illumination with light. As the fluorescent granule profiles can disappear after exposure to strong ultraviolet light for 10 sec [6], they provide a measure of possible photo-bleaching effects. In addition, as these cells are located in the Space of Disse region within the sinusoids, they provide a morphological guide to the location of blood flowing through the liver. Figure 5b shows a corresponding image of the liver with multiphoton tomography. A lower intensity for these fluorescent granules is evident and is consistent with the optical sectioning property of multiphoton to-

Journal of
BIOPHOTONICS

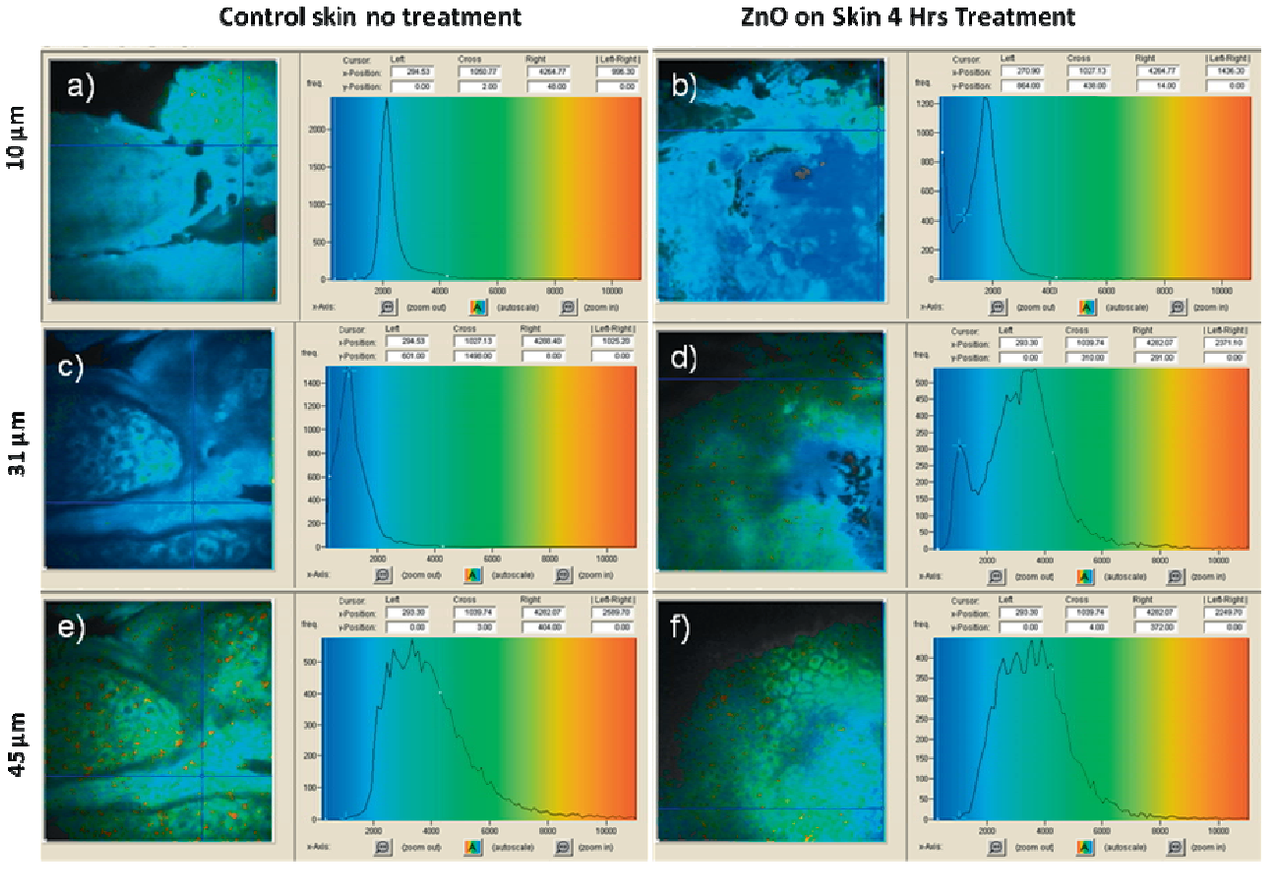

Figure 4 (online colour at: www.biophotonics-journal.org) *In vivo* control and treated skin after exposure of zinc oxide for 4 hrs intensity versus life times for zinc oxide, stratum corneum and viable epidermis. 740 nm excitation, channel 1 (350–415 nm), field of view 175 : 175 µm. a) stratum corneum control; b) stratum corneum after zinc oxide application for 4 hr; c) first layer of viable epidermis control; d) first layer of viable epidermis after zinc oxide application for 4 hr; e) viable epidermis control and f) viable epidermis after zinc oxide application for 4 hr.

mography compared to the intravital fluorescence microscopy approach that captures off-focal plane fluorescence. Consequently, Figure 5 highlights a key difference between the epi-fluorescent full-field (intravital) microscopy (Figure 5a) and multiphoton tomography techniques (Figure 5b). The intravital microscopy captures more fluorescence signal from the greater off-focal plane tissue layers, whereas multiphoton tomography imaging depth is limited to the optical section thickness (measured to be 2 µm). The latter gives a better resolution of cell characteristics.

Figure 6 shows representative reference pictures for changes in liver fluorescence after fluorescein injection using intravital microscopy as reported by Hanzon [6]. It is evident that the cells show an increase in fluorescence whereas the sinusoidal (blood vessel) regions remain relatively black. At longer times, there is clear evidence of fluorescein excretion into the bile and that the bile ducts exist between the cells.

In our work using multiphoton tomography, an increase in fluorescence was associated with fluorescein administration but the extent of differentiation with the background was not as profound. Excellent differentiation was found when a higher resolution objective lens (×40) was used. However, this use also resulted in a loss in the field of vision. As a consequence, emphasis was placed on being able to increase the resolution of fluorescein fluorescence from that of the endogenous background using FLIM. Whilst free fluorescein has a lifetime of about 4 ns, fluorescein has a lower lifetime when in an uncharged, mono-anion or bound form. Figure 7 shows the fluorescence lifetimes observed in the liver in the presence of fluorescein. It is obvious that the fluorescein injection resulted in a several-fold increase in fluorescence signal as defined by photon counting using FLIM. In addition, an initial mean tissue fluorescence lifetime τ of approximately 1.7 ns (Figure 7c), characteristic of that of endogenous tissue τ (dominated by t of NAD[P]H), increased to τ

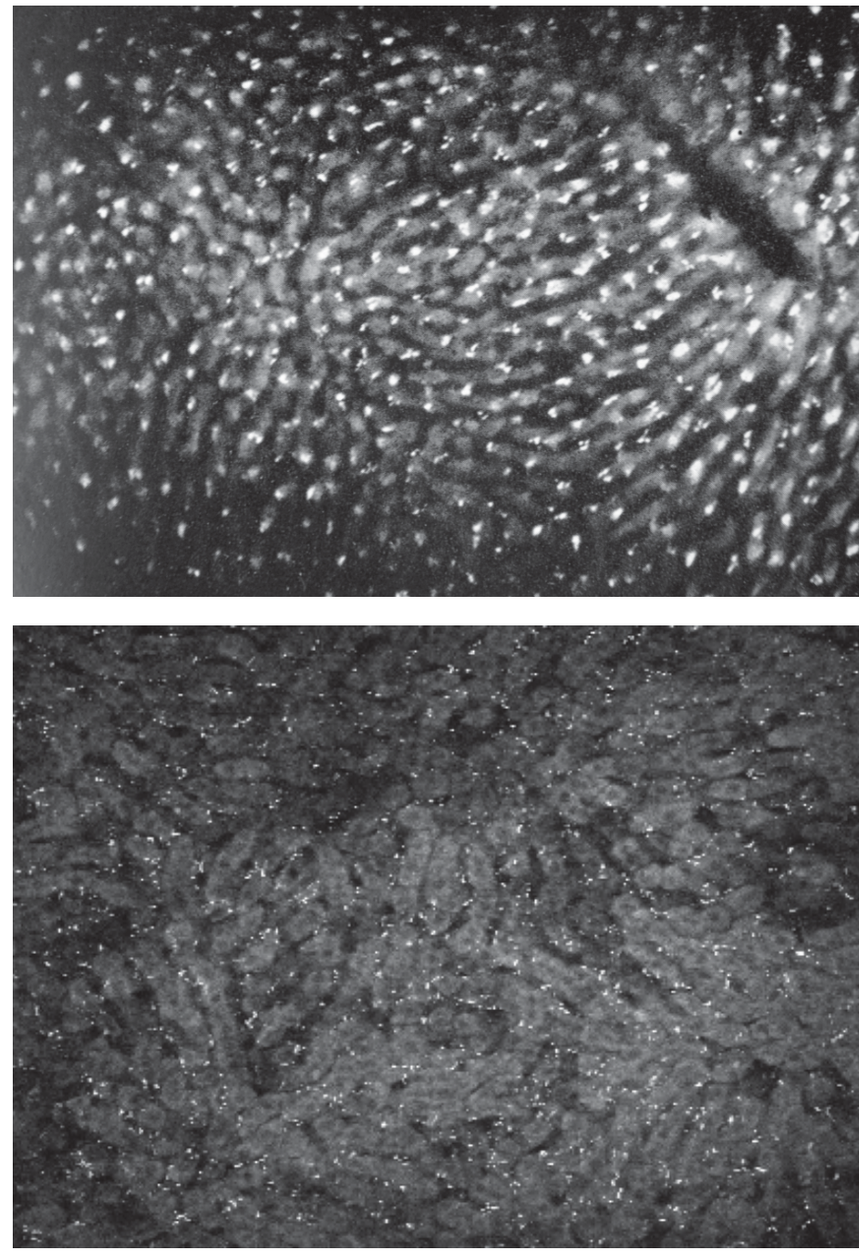

Figure 5 Autofluorescence of liver seen with a) intravital fluorescence microcopy (×45) from Hanzon [6] and b) by *in vivo* multiphoton microscopy, excitation 750 nm, BG39 (350–650 nm), field of view 620 : 620 μm.

about 2.9 ns, indicative of fluorescein being present. The lower lifetime than the reported value of $\tau = 4.1$ ns for fluorescein in solution most likely has arisen from fluorescein being in the liver mainly in a bound form that will result in a shorter fluorescence lifetime FLIM enabled imaging of fluorescein in the bile in a manner not possible using band pass filters alone. The bile duct pattern observed after intravital fluorescence microscopy (Figure 6d) is less clear in our multiphoton tomography (Figure 7). The difference would again be consistent with multiphoton tomography taking an "optical section" in the focal plane, resulting in a fragmented bile duct image depending on whether the duct was in or out of the focal plane. In our studies, the lifetime for 2 μg/mL fluorescein (Tris 50 mM buffer pH 8) in Channel 2 (450 nm–515 nm) was 3.5–3.7 ns.

A mean lifetime for the fluorescein present in bile collected from livers 20 min after fluorescein injection *in vivo* was ~2.7 ns. This lifetime peak was absent in control bile and the bile was found to have a pH of 7.7. The relative amount of fluorescein and fluorescein glucuronide in bile 20 min after fluorescein injection was 3 : 1 based on the HPLC relative peak area detected at 480 nm. A molecule with properties (HPLC retention time, visible and fluorescence spec-

Journal of
BIOPHOTONICS

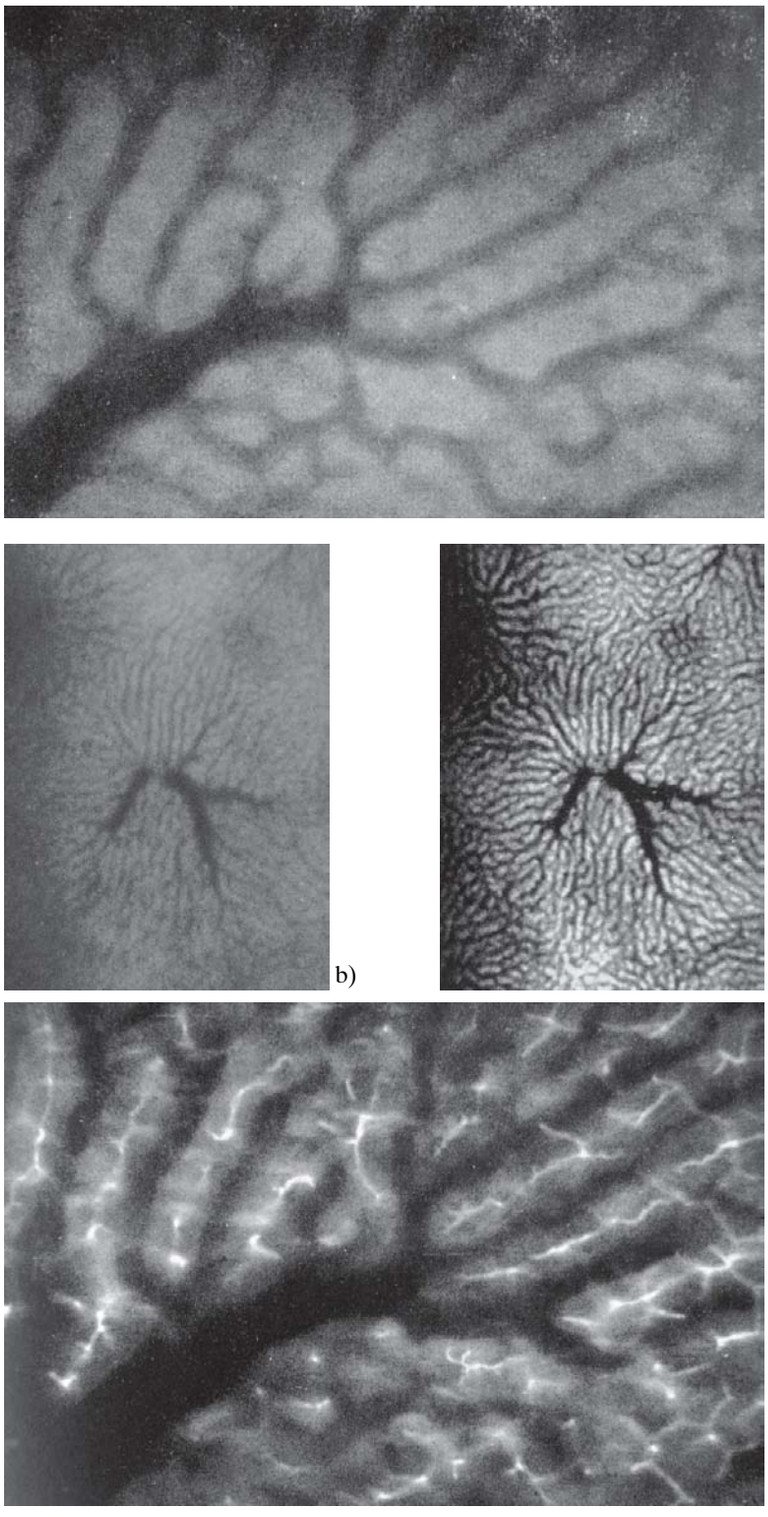

Figure 6 Fluorescein disposition in normal liver with intravital fluorescence microscopy. a) Autofluorescence of liver (×300); b) Autofluorescence of liver (×30); c) 6min after fluorescein injection (X30); d) 8 min after fluorescein injection (×300). From [6].

tra, fluorescence lifetime) corresponding with fluorescein glucuronide has a fluorescence lifetime of 2 ns when mixed with crude liver homogenate at pH 7. Bile spiked with fluorescein has two life time components at 3370 ps (30%) and 3782 ps (11%) suggesting a protein bound and unbound component. Bile spiked with the fluorescein glucuronide also had two life time components but these had shorter life times than fluorescein in bile. The fluorescein glucuronide lifetimes in bile are 2240 ps (11%) and 2480 ps (29%).

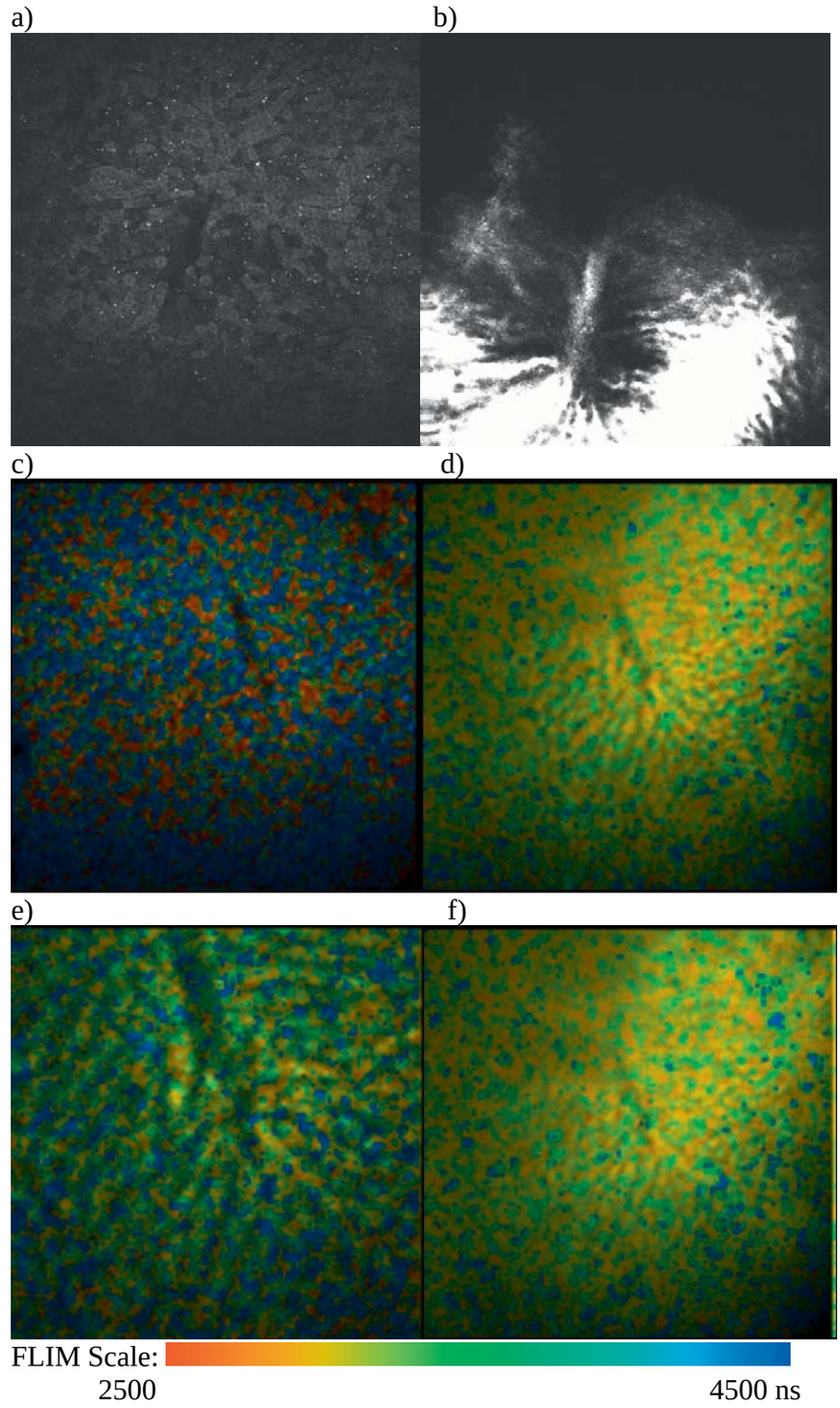

Figure 7 (online colour at: www.biophotonics-journal.org) Fluorescein disposition in normal liver. The FLIM images show channel 2 (450–515 nm). a) Autofluorescence of liver by multiphoton microscopy at 750 nm (filter BG39), b) liver seen 10 seconds after fluorescein injection by multiphoton microscopy (filter FDIG) at 920 nm, FLIM (filter BG39) of c) control liver (photon count 2000, field of view 620 : 620 μm, 750 nm excitation), d) 3 min after injection of fluorescein (photon count 22000, 750 nm excitation, field of view 620 : 620 μm) e) 12 min after injection of fluorescein (photon count 7000, 750 nm excitation, field of view 293 : 293 μm); and f) 2 min after fluorescein injection (920 nm excitation, field of view 620 : 620 μm).

4. Discussion

4.1 ZnO and skin

Skin has a number of endogenous skin fluorophores with the following characteristics (excitation wavelength, nm; emission wavelength, nm; fluorescence lifetime, ns): [21, 22] (Table 1). In our work, we used a band pass filter at 380 ± 10 nm (its FWHM is 20 nm) to take advantage of the differences in zinc oxide emission fluorescent properties compared to endogenous skin spectra. As shown in Figure 2a, this band pass is outside that of epidermal spectra and indicates that ZnO with-

Journal of
BIOPHOTONICS

Table 1 Endogenous skin fluorophores and characteristics [21, 22].

Endogenous fluorophore	Excitation wavelength (nm)	Emission wavelength (nm)	Fluorescence lifetime (ns)
NAD(P)H	290/340/350	440–470	0.3/2.3
Flavines	370/450	430	5.2
Elastin	290–340	420–460	0.2–2.5
Collagen	300–340	420–460	0.2–2.5
SHG Collagen	750–850	375–425	<0.050
Melanin	uv/visible, 466	430/440/545/520/555/575	0.2/1.9/7.9
PPIX	405/630	635/710	11
Keratin	~800	525	1.6

out endogenous fluorescence from the epidermis can be seen in this range of emission wavelengths.

The ability to distinguish zinc oxide from the epidermis using the fluorescent lifetimes for zinc oxide proved to be more difficult than anticipated. The long decay lifetimes were not readily useable with the pulsing of 75 fs provided by the Mai Tai laser. In addition, the fluorescent lifetime at 1.036 ns is similar to that of pure keratin and 289 ps similar to 0.2 to 0.4 ns observed for keratin in hair [23]. Fluorescent lifetimes in viable epidermis were in the range of 1.8 to 2.4 ns, with mitochondrial bound NAD(P)H having a typical lifetime of 2 to 3 ns [21]. However, given the flavine lifetime of 5.2 ns, the zinc oxide lifetime of 4.3 ns may lead to overlap. The best way of using FLIM to resolve zinc oxide from endogenous auto fluorescence is then to use a combination of selective wavelengths and FLIM. It is evident that of the four emission wavelength channels available with FLIM: $1 = 350–450$ nm; $2 = 450–515$, $3 = 515–620$ and $4 = 620–670$, that channel 1 allows the use of FLIM in a selective manner. The analysis in Figure 3 shows that the selectivity obtained was similar to that found with the band pass and provided further confirmation that zinc oxide was only retained in the skin furrows and did not penetrate deeper. In Figure 4b–c there is evidence of ZnO in viable epidermis, however in the false colored imaged (4d) no cells can be visualized, indicating that the location might be in stratum corneum rather than in viable epidermis.

Studies on ZnO transport into different regions of the skin showed no evidence of elemental Zn in control samples (not treated with CCT-60 ZnO). The normal elemental Zn background levels in skin ranges from 4.5–6.7 ppm [24], much lower than the detection limit of the SEM EDX instrument of between 200–1000 ppm [25].

4.2 Liver studies

The liver is the key organ for the detoxification of foreign compounds that enter the body. Although the pharmacokinetics of such compounds is well studied, they are generally limited to a global description based on *ex vivo*, cell culture and liver perfusion studies. Multiphoton tomography allows the precise events associated with solute disposition in liver cells to be studied both in space and in time. Traditional intravital fluorescence microscopy studies are limited in the ability of being able to precisely quantify changes in either drug or in metabolites due to the dominant role of liver auto fluorescence. In this study we showed that multiphoton tomography is an excellent method to study the 'real' *in vivo* condition in the liver and skin. In the skin it can be used to study penetration of drugs whereas in the liver the metabolism and elimination of drugs into bile can be visualized. Liu et al used detection bandwidths of 390 ± 10, 460 ± 25, 525 ± 25, and 590 ± 40 nm to measure second harmonic generation, stellate cells, 6-carboxyfluorescein diacetate and rhodamine B isothiocyanate-dextran 70,000 fluorescence, respectively [10].

We chose fluorescein for these liver studies as it is one of the most widely studied fluorescent molecules. In addition, the transport of fluorescein in the liver has been described by intravital fluorescence microscopy [6, 26, 27]. In the present study, we used a range of doses of fluorescein. Both the spatial and temporal disposition of fluorescein depended on the dose employed. For instance, with low doses, FLIM images (excitation 750 nm) revealed fluorescein in only 20% of the field of view, being most evident in the periportal region and appeared to be saturated with fluorescein within 2 minutes post-injection. At higher doses, as shown in Figure 7, the entire field of view was saturated with fluorescein within 2 minutes post-injection. At high doses, as also reported by others, fluorescein is retained in the liver for up to 1 hr. During this time, zone 1 or the periportal region of the liver is the first to become fluorescein free (dark). Zone 3 (centrilobular and pericentral) region often has significant fluorescein levels present at 1 hour [24, 27].

Our data also provides evidence that a drug and metabolite have different lifetimes in the various regions of the liver *in vivo*. For instance, collected rat bile

had a pH of 7.7, a pH in which fluorescein will exist in the dianionic form with a fluorescence lifetime of about 4.1 ns or higher [28, 29] compared to 3.8 ns at lower pH values. However, the average observed lifetime observed for bile after fluorescein administration was 2.7–2.9 ns, indicating other confounding influences were present. One of these is that about half of the fluorescein excreted into the bile will be as the fluorescein monoglucuronide [30], and this has a lower fluorescent lifetime of ∼2.3 ns [31]. In the present work, we found that about 25% of the fluorescein in the bile was in the glucuronide form and that the fluorescein glucuronide did have a lower lifetime than fluorescein itself. Further, fluorescein and its monoglucuronide are known to be highly protein bound e.g. fluorescein ∼89% in plasma [32], fluorescein monoglucuronide 59% [33] and that bile contains a number or proteins [34]. The two life time components at 3370 ps (30%) and 3782 ps (11%) for bile spiked with fluorescein may reflect the presence of a protein bound and an unbound component as could also the two shorter life time components for bile spiked with the fluorescein glucuronide (2240 ps (11%) and 2480 ps (29%)). However, as mentioned earlier, the dependence of fluorescein lifetime on the local pH [28, 29] may also lead to a variation in fluorescent lifetimes. The combination of all lifetimes is consistent with an overall mean lifetime found in bile after fluorescein administration of about 2.7–2.9 ns. A lower fluorescence lifetime for protein bound fluorescein and protein bound form of its monoglucuronide metabolite may be attributed to a Förster resonance energy transfer (FRET) between the fluorescein and its metabolite with the proteins present. Further analyses are presently being undertaken to use the different fluorescent lifetimes evident after fluorescein injection in Figure 7 to understand the physiological pharmacokinetics of fluorescein in the liver.

5. Conclusion

In vivo multiphoton tomography has been used to examine the transport of zinc oxide nanoparticles in human skin and fluorescein disposition in rat liver with both band pass fluorescence and FLIM. The analysis shows that the zinc oxide nanoparticles examined did not penetrate into the viable epidermis and that multiphoton tomography could be used to give similar results as reported previously for intravital fluorescence microscopy but with a greater resolution.

Acknowledgements We acknowledge the support of the Australian National Health & Medical Research Council and the Lions Medical Research Foundation in undertaking this work.

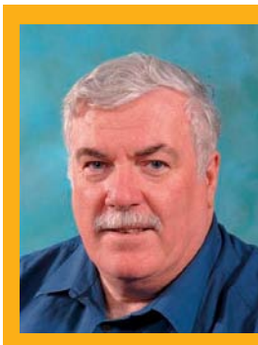

Michael Stephen Roberts is a NHMRC Senior Principal Research Fellow & Director, Therapeutics Research Unit in the School of Medicine at the University of Queensland, in Brisbane, Australia. His key research areas of interest are rational drug design, drug delivery by the skin, pharmacokinetics and quality use of medicines. Professor Roberts is Guest Editor for Drug Discovery Today, Associate Editor of Skin Pharmacology and Applied Physiology and a Member of Editorial Boards for Journal of Pharmacokinetics & Pharmacodynamics, Current Drug Delivery, Clinical Pharmacokinetics and Pharmaceutical Research. He has been Co Chair, Gordon Research Conference on Barrier Function of Mammalian Skin, in Rhode Island and served as Chair, World Health Organisation (WHO) Committee's International Program on Chemical Safety Environmental Health Committee Task group, which met in Hanover Germany.

Matthew Roberts, BSc, is a research assistant in the Therapeutics Research Unit and is studying medicine at the University of Queensland. He was awarded the Royal Australasian College of Surgeons Dissection Prize and has helped establish the multiphoton studies of the liver in vivo.

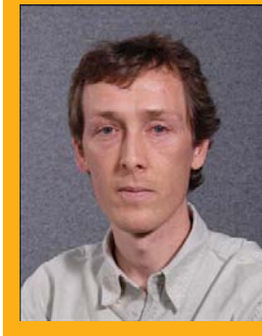

Thomas A. Robertson graduated with Honours in Chemistry from the University of Adelaide in 1991 and received his Ph.D. in Organic Chemistry from the Australian National University in 1997. Between 1997 and 2001 he studied enzyme mechanisms with Professor Tim D.H. Bugg at the University of Southampton and peptidomimetic drug design and synthesis with Professor R. Kip Guy at the University of California, San Francisco. Since 2001, he has worked at the University of Queensland and previously studied synthetic peptidomimetics and synthetic vaccines. His current fields of scientific interest include: analytical chemistry, antithrombotic drug development and novel applications of multi-photon microscopy.

Journal of
BIOPHOTONICS

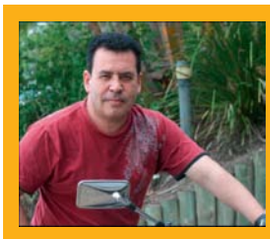

Washington H. Sanchez graduated from Monash University in 1998 (BAppSci Chem), Queensland University of Technology (MApp Sci Chem 2001, PhD 2006). He spent the first three years after his graduation in industry as a manger for a multinational science solutions company. He has also performed various consulting roles in industry where his analytical skills were sought predominantly in the polymer science area. He joined the University of Queensland where he is currently one of the senior research officers for the Therapeutic Research Unit under Prof. Michael Roberts. Currently he holds an emeritus researcher position at the Queensland University of Technology, with Professor Graeme George, director of CRC for Polymers node. His expertise includes polymer chemistry, electron microscopy, mass spectrometry and vibrational spectroscopy. His research interests are polymer chemistry in scar remediation, nanoparticles drug delivery and wound healing.

Camilla A. Thörling graduated with a Master of Pharmacy from the University of Gothenburg, Sweden in 2007. She came to Australia in July 2006 to complete a research project at the School of Biomedical Sciences, The University of Queensland. In 2007 she returned to Sweden to fulfill the supervised training requirements of her degree in the largest retail pharmacy in Gothenburg. She gained employment in the Therapeutics Research Unit, School of Medicine at The University of Queensland in April 2008. Her active projects involve skin and liver studies, working with Multiphoton Tomography. Her interests include liver pharmacology and morphology as well as fluorescence and electron microscopy.

Xin Zhao is a PhD student in Biophysics of Division of Information and Communication Sciences, Macquarie University, Sydney, Australia supervised by Andrei Zvyagin. During March 2006 to December 2007, she worked closely with the researchers in Therapeutic Research Unit, supervised by Professor Miichael Roberts. In the first half of her PhD study, she did research in University of Queensland, from which she also got her Master degree in Biomedical Engineering in 2005. In July of 2007, she transferred her degree to Macquarie University and is going to graduate in the beginning of 2009.

Yuhong Zou is an Australian National Health & Medical Research Council (NHMRC) research officer, Therapeutics Research Unit in the School of Medicine at the University of Queensland, in Brisbane, Australia. Dr. Zou is an invited reviewer for several international and Chinese medical journals. His current key research areas of interest are drug delivery, pharmacokinetics in rat liver diseases model. He has been active in pathogenesis and treatment of liver diseases (acute liver injury, liver fibrosis and nonalcohol liver diseases) since 2000 and has over 20 papers published.

Wolfgang Becker is a specialist in time-resolved optical detection techniques. He obtained his PhD 1979 in Berlin, Germany. Since 1993 he is the head of Becker & Hickl GmbH in Berlin. His field of interest is development and application of time-correlated single photon counting techniques.

Andrei V. Zvyagin received his Diploma from the Moscow Engineering Physics Institute, Russia, and the PhD degree in Engineering from the Tokyo Institute of Technology in 1997. He spanned a range of positions from an Engineer to Senior Research Scientist in the Institute of Metrology for Time and Space, Moscow, Russia. From 1998 to 2004, he was an Australian Postdoctoral Fellow in the Optical and Biomedical Engineering Laboratory, The University of Western Australia, studying optical coherence tomography for biomedical imaging applications. From 2004–2007, he joined The University of Queensland as a Lecturer/Senior Lecturer. From 2007, Dr Zvyagin is Associate Professor, Macquarie University, Sydney, Australia. His research interests include various areas of Biophotonics and Nanotechnology, like optical scanning near-field microscopy, optical coherence-domain imaging, non-linear optical microscopy, molecular-label assisted optical biological imaging.

References

[1] Y. Dancik, O. G. Jepps, and M. S. Roberts. Physiologically Based Pharmacokinetics and Pharmacodynamics of Skin, In M. S. Roberts and K. A. Walters (eds.), Dermal Absorption and Toxicity Assessment, Informa Healthcare, 2007.
[2] D. Y. Hung, P. Chang, M. Weiss, and M. S. Roberts, J. Pharmacol Exp Ther **297**, 780–789 (2001).
[3] K. S. Pang and M. Rowland, J. Pharmacokinet. Biopharm. **5**, 625–653 (1977).
[4] M. S. Roberts and M. Rowland, J. Pharmacokinet. Biopharm. **14**, 227–260 (1986).
[5] P. Ellinger, Biological Reviews **15**, 323–347 (1940).
[6] V. Hanzon, Acta Physiol Scand Suppl **28**, 1–268 (1952).
[7] M. D. Mengerand and H. A. Lehr, Immunol Today **14**, 519–522 (1993).
[8] B. Yu, K. Hean Kim, P. T. So, D. Blankschtein, and R. Langer, J Invest Dermatol **118**, 1085–1088 (2002).
[9] F. Stracke, B. Weiss, C. M. Lehr, K. Konig, U. F. Schaefer, and M. Schneider, J Invest Dermatol **126**, 2224–2233 (2006).
[10] Y. Liu, H. C. Chen, S. M. Yang, T. L. Sun, W. Lo, L. L. Chiou, G. T. Huang, C. Y. Dong, and H. S. Lee, J. Biomed. Opt. **12**, 014014 (2007).
[11] K. W. Dunnand and T. A. Sutton, ILAR J. **49**, 66–77 (2008).
[12] K. Schenke-Layland, I. Riemann, O. Damour, U. A. Stock, and K. Konig, Adv. Drug. Deliv. Rev. **58**, 878–896 (2006).
[13] K. König, Clinical multiphoton tomography Journal of Biophotonics **1**(1) 13–23 (2008).
[14] S. E. Cross, B. Innes, M. S. Roberts, T. Tsuzuki, T. A. Robertson, and P. McCormick, Skin. Pharmacol. Physiol. **20**, 148–154 (2007).
[15] J. P. Ryman-Rasmussen, J. E. Riviere, and N. A. Monteiro-Riviere, Toxicol. Sci. **91**, 159–165 (2006).
[16] W. Becker, Advanced Time-Correlated Single Photon Counting Techniques, Springer (2005).
[17] Becker & Hickl GmbH, DCS-120 Confocal Scanning FLIM Systems, available on www.becker-hickl.com.
[18] K. Konig, A. Ehlers, F. Stracke, and I. Riemann, Skin. Pharmacol. Physiol. **19**, 78–88 (2006).
[19] A. V. Zvyagin, X. Zhao, W. Sanchez, J. A. Ross, M. S. Roberts, Imaging of Zinc Oxide Nanoparticle Penetration in Human Skin in vitro and in vivo. J. Biomed. Opt. (in press).
[20] H. S. Lee, Y. Liu, H. C. Chen, L. L. Chiou, G. T. Huang, W. Lo, and C. Y. Dong, Opt. Lett. **29**, 2614–2616 (2004).
[21] K. Konig and I. Riemann, J. Biomed. Opt. **8**, 432–439 (2003).
[22] W. Becker, A. Bergmann, E. Haustein, Z. Petrasek, P. Schwille, C. Biskup, L. Kelbauskas, K. Benndorf, N. Klocker, T. Anhut, I. Riemann, and K. Konig, Microsc. Res. Tech. **69**, 186–195 (2006).
[23] A. Ehlers, I. Riemann, M. Stark, and K. Konig, Microsc. Res. Tech. **70**, 154–161 (2007).
[24] R. I. Gorodetsky, J. Sheskin, A. Weinreb. Iron, Copper, and Zinc Concentrations in Normal Skin and in Various Nonmalignant and Malignant Lesions. Int. J. Dermatol. **25**, 440–445 (1986).
[25] S. Steinbrecher and E. Plies. Improving the X-Ray Fluorescence Analysis in the SEM; Microsc. Microanal. **9** (Suppl. 3), 158–159 (2003).
[26] J. J. Gumucio, D. L. Miller, M. D. Krauss, and C. C. Zanolli, Gastroenterology **80**, 639–646 (1981).
[27] I. A. Sherman and M. M. Fisher, Hepatology **6,** 444–449 (1986).
[28] M. Hammer, D. Schweitzer, S. Richter, and E. Konigsdorffer, Physiol. Meas. **26**, N9–12 (2005).
[29] H. B. T. Sanjay Pant and D. D. Pant, Journal of Photochemistry and Photobiology A: Chemistry **81**, 7–11 (1994).
[30] F. Holzinger, C. D. Schteingart, H. T. Ton-Nu, S. A. Eming, M. J. Monte, L. R. Hagey, A. F. Hofmann. Fluorescent bile acid derivatives: relationship between chemical structure and hepatic and intestinal transport in the rat. Hepatol. **26**, 1263–71 (1997).
[31] M. Larsen and L. B. Johansson, Time-resolved fluorescence properties of fluorescein and fluorescein glucuronide. Exper, Eye, Res. **48**, 477–85 (1989).
[32] M. B. Affrime, D. L. Blecker, P. J. Lyons, J. M. Pitone, C. D. Swartz, and D. T. Lowenthal. The effect of renal transplantation on plasma protein binding. J. Dialysis. **3**, 207–18 (1979).
[33] C. Seto, M. Araie, and M. Takase, Binding of fluorescein and fluorescein-monoglucuronide to proteins. Atarashii. Ganka. **2**, 387–9 (1985).
[34] T. Osnes, O. Sandstad, V. Skar, M. Osnes, and P. Kierulf. Total protein in common duct bile measured by acetonitrile precipitation and a micro bicinchoninic acid (BCA) method. Scand J Clin Lab Invest. **53**, 757–63 (1993).